A Multiscale model validated on local current measurements for understanding the solid oxide cells performances

E. da Rosa Silva, G. Sassone, M. Prioux, M. Hubert, B. Morel, J. Laurencin

A Multiscale model validated on local current measurements for understanding the solid oxide cells performances

E. Da Rosa Silva[1], G. Sassone[1], M. Prioux[1], M. Hubert[1], B. Morel[1], J. Laurencin[1,*]

(1) Univ. Grenoble Alpes, CEA/LITEN, 17 Avenue des Martyrs, 38054 Grenoble/France

Abstract. A physical-based model has been developed and validated to unravel the complex relationships between the global solid oxide cells response and the reaction mechanisms taking place in the electrodes. This numerical tool combines three length-scales modules from the electrode microstructure up to the single repeat unit. This model allows computing the local distribution of reaction kinetic rates, current densities, and gas composition as function of the cell operating conditions. To validate the multiscale model, a special experimental setup has been developed to measure the local polarization curves along the cell length. For this purpose, a specific design of the interconnect has been proposed in order to probe the local current density on standard cells. A good agreement has been found between the experimental and simulated data for different operating conditions. The fully validated model has been used to analyze the cell operation in electrolysis and fuel cell modes. The activated reaction pathways associated with the elementary steps in the active layers have been investigated depending on the position along the cell length.

Keywords. Solid Oxide Electrolysis Cell, Solid Oxide Fuel Cell, Multiscale Modeling, Local Polarization Curves.

*Corresponding author: Telephone: +33 4 38 78 22 10,

E-mail: jerome.laurencin@cea.fr

1. Introduction

In a scenario with growing energy demand and a tendency to reduce fossil fuel consumption, hydrogen is considered as an important energy vector for the transition toward a low-carbon energy market [1]. In this context, High-Temperature Steam Electrolysis (HTSE) based on Solid Oxide Cells (SOCs) technology presents a great potential to produce H_2 at a low cost and high efficiency [2]. SOCs are electrochemical devices that can operate in fuel cell mode (SOFC) and electrolysis mode (SOEC) with a large range of fuels and no utilization of expensive catalysts [3]. Due to its reversibility, this technology can also be used to match the fluctuations between electricity demand and production, mainly during the consumption peaks [4]–[6]. Classical SOCs are composed of a dense electrolyte sandwiched between two porous electrodes. The reactions of hydrogen oxidation and steam reduction occur in the fuel electrode (Eq. 1a), whereas the oxygen is consumed or produced in the air electrode (Eq. 1b). A porous Nickel and Yttria-Stabilized Zirconia (Ni-YSZ) cermet is typically used for the fuel electrode, while the air electrode is composed of a Mixed Ionic and Electronic Conductor (MIEC). Nowadays the most common material for the air electrode is a composite of Lanthanum Strontium Cobalt Ferrite ($La_xSr_{1-x}Co_yFe_{1-y}O_{3-\delta}$ - LSCF) and Gadolinium-doped Ceria ($Gd_xCe_{1-x}O_{2-\delta}$ - CGO) [3], [7], [8]. The electrolyte is a pure ionic conductor, which allows the migration of oxygen vacancies ($V_O^{\bullet\bullet}(YSZ)$), and it is usually made of Yttria-Stabilized Zirconia with 8.mol% of yttria (8YSZ) [9].

$$H_2(g) + O_o^x(YSZ) \underset{SOEC}{\overset{SOFC}{\rightleftarrows}} H_2O(g) + V_o^{\bullet\bullet}(YSZ) + 2e^- \quad [1a]$$

$$\frac{1}{2}O_2(g) + V_o^{\bullet\bullet}(YSZ) + 2e^- \underset{SOEC}{\overset{SOFC}{\rightleftarrows}} O_o^x(YSZ) \quad [1b]$$

To reach economic viability, the cell performances still need to be improved while the degradation rate should be limited to 0.5 %.kh^{-1} in SOEC mode (for an operating current density of -1.5 A.cm^{-2} [10]) and 0.2 %.kh^{-1} in SOFC mode [11]. However, degradation rates measured at current densities lower than 1 A.cm^{-2} have been reported in the literature in the range of 1 – 3 %.kh^{-1} [12] and 2 – 10 %.kh^{-1} [13] for SOFC and SOEC operation, respectively. Degradation phenomena can be caused by different factors such as microstructural evolution, electroactive site poisoning, and chemical decomposition [14]. Those phenomena can be aggravated by harsh operating conditions at high current density and/or high fuel utilization/steam conversion, which can result in strong gradients of concentration along the cell length.

In general, the electrochemical characterization techniques (e.g. polarization curves and Electrochemical Impedance Spectroscopy (EIS)) are used to measure the global cell response without any information on the spatial distributions arising in the electrodes [7]. Hence, current inhomogeneities that are associated with locally-critical conditions are not detected. To overcome this limitation, specific experimental setups must be designed for local electrochemical analyses. The most extensively applied method for local measurements is the electrode segmentation [15]–[22]. It consists in the segmentation of the air electrode into small disconnected zones, which are electronically isolated from each other. For this purpose, the electrode layer is printed over the entire surface of the electrolyte in insulated segments, allowing the measurements in distinct areas of the cell [7], [20].

Although the electrode segmentation technique has been extensively applied for other types of cells (e.g. proton exchange membrane fuel cells), the same abundant quantity of data is not found for SOCs application [17], [23]. This under-utilization of segmented cells for the high temperature applications lies in difficulties to change the design of the air electrode and to probe the current and/or temperature in each segment. Besides, the air electrode partitioning can induce heterogeneities of current and potential that can affect the cell behavior [17]. Hence, new experimental facilities must be developed to perform local analysis using standard cells by avoiding any type of modification in the cell geometry.

The relevance of spatially resolved electrochemical measurements can be significantly enhanced when applied in combination with mathematical modelling. Indeed, the simulation also gives the possibility to have an access to local parameters that are not easily measured (e.g. partial pressures repartition inside the porous media or distribution of overpotentials along the cell length) [17], [20], [21]. In this sense, numerical modeling of SOCs is becoming crucial for a deeper insight into the processes that occur within the electrodes. Accordingly, a significant number of models have been presented in the literature with different approaches and length scales.

For instance, mathematical models have been developed to emulate representative electrode microstructures [24]–[26]. These models can be useful to identify microstructural corrections that control the electrode efficiency [26]. In terms of electrochemical response, some microscale electrochemical models have been proposed to describe precisely the electrode reaction mechanism including mass and charge transfer within the active functional layer [3], [27]–[30]. On the other hand, many macroscale models have been developed to take into account the full geometry of the single repeating unit (SRU) [23], [31], [32] or stack [33]–[35]

including the complete cell, the flow channel and the interconnect. As a general matter, these macro-models present a rather simplified description of the reaction mechanisms, whereas a special attention is paid to describe accurately the fluid distribution in the system and how it can affect the performances.

One possibility to increase the complexity of the SOCs models is to combine the different length scales in a multiscale approach [4]. Complex descriptions from a microscale approach (e.g. microstructure emulation and complex reaction mechanisms) can be coupled with the macro description to better understand the role of microstructure and the reaction mechanism on performances and degradation. In the recent years, some multiscale models have been developed for the SOCs application [33], [36]–[40], showing the power and the potential of these numeric tools. However, it is still necessary to develop an integrated model including (i) a microstructural description of the electrodes, (ii) a decomposition of the reaction pathways in pure elementary steps for both electrodes and (iii) a global description of the SRU geometry. Moreover, despite all the works dedicated to the SOCs modeling in the literature, only a small quantity of them [41]–[43] have bridged the multiscale approach to a spatial resolved electrochemical analysis. To the best of our knowledge, only the group of G. Schiller have published a series of articles, in which a multiscale model [44] was applied to analyze the local polarization curves acquired in a segmented setup [41]–[43].

In this work, a coupled experimental and multiscale model approach has been proposed in order to unravel the relationships between a classical SOC response and the mechanisms that take place in the electrodes. The multiscale model is composed of three different length-scale modules. The first one emulates digital twins of the electrode microstructure, giving the possibility to have a complete description of the morphology of the electrodes. It is linked to two microscale models for both electrodes. They take into consideration the reaction mechanisms in a sequence of pure elementary steps associated with charge and mass transport phenomena in the active layers. Finally, all the modules are linked to a macroscopic description that takes into account the SRU design including the gas channels. The multiscale model has been validated using global and local polarization curves using a standard cell (i.e. fuel electrode supported cell made of the classical materials). For this purpose, an innovative design of the air electrode interconnect is proposed in order to probe the local distribution of the current without any kind of electrode segmentation. After validation, the model has been used to analyze the evolution of the reaction mechanism in the electrode along the cell length.

2. Materials and methods

2.1 Cell description

In this study, a 'standard' fuel electrode-supported cell was studied. The cell has a circular shape with an active area of 9.08 cm^2. A thin and dense electrolyte made of 8YSZ with a thickness of 8 µm was sandwiched between two porous electrodes. The air electrode is a bilayer with a current collector made of LSCF (ca. 20 µm tick) and an active layer in LSCF-CGO (ca. 20 µm thick). A 3 µm barrier layer of CGO is inserted between the electrolyte and the air electrode to avoid the formation of secondary phases. The fuel electrode is composed a thin functional layer in Ni-8YSZ (ca. 25 µm) and a thick support layer (ca. 280 µm) made of Ni-3YSZ cermet.

2.2 Setup description

All tests were carried out in an in-house test bench depicted in Figure 1a. The circular cell is positioned in a metallic housing. Both anodic and cathodic gases are introduced at the cell center and are distributed along the electrodes in a radial co-flow configuration. The inlet gas fluxes are delivered by mass flow controllers (Brooks SLA5850S).

On the fuel side, a Ni grid (100 meshes.cm^{-2}) is used to collect the current at the electrode surface. A ceramic glass seal (Schott G018-311) is deposited on the edge of the cell to ensure the gas tightness of the hydrogen compartment. It can be noticed that steam is produced using a steam generator operated in saturated vapor conditions. In parallel, hydrogen is introduced and mixed with the steam before entering the cell. At the cell outlet, a heat exchanger allows separating the water from the dry gas.

At the air side, a specific design of the metallic interconnect is applied in order to measure the local current distribution along the cell radius. This setup is made of Inconel Ni-based alloy and its geometry is displayed in Figures 1b and 1c. The metallic support is divided into numerous pins that are positioned from the gas inlet to the edge of the electrode. Nine of those pins are drilled to allow the passage of wires that are welded in the extremity of each pin. Another wire is welded to the opposite surface of the interconnect and used as a reference for the voltage measurement. With this configuration, when a current density is imposed to the cell under operation, the voltage drop can be measured for each pin. Since the geometry and the electrical conductivity of the interconnect material is known precisely, it is possible to calculate accurately the local current density passing through by each pin (corresponding to the local current collected by the pin on the electrode). Hence, this modification in the

interconnect geometry offers the advantage to perform local current measurements (and consequently, local polarization curves) using classical cells without any specific segmentation of the air electrode [15]–[17], [19], [45]. Finally, it is worth mentioning that two gold grids (100 meshes.cm^{-2}) with a diameter of 34 mm are inserted between the interconnect and the electrode surface to improve the electrical contact. Moreover, a mechanical pressure of 600 g.cm^{-2} is also applied on the setup to further decrease the contact resistances.

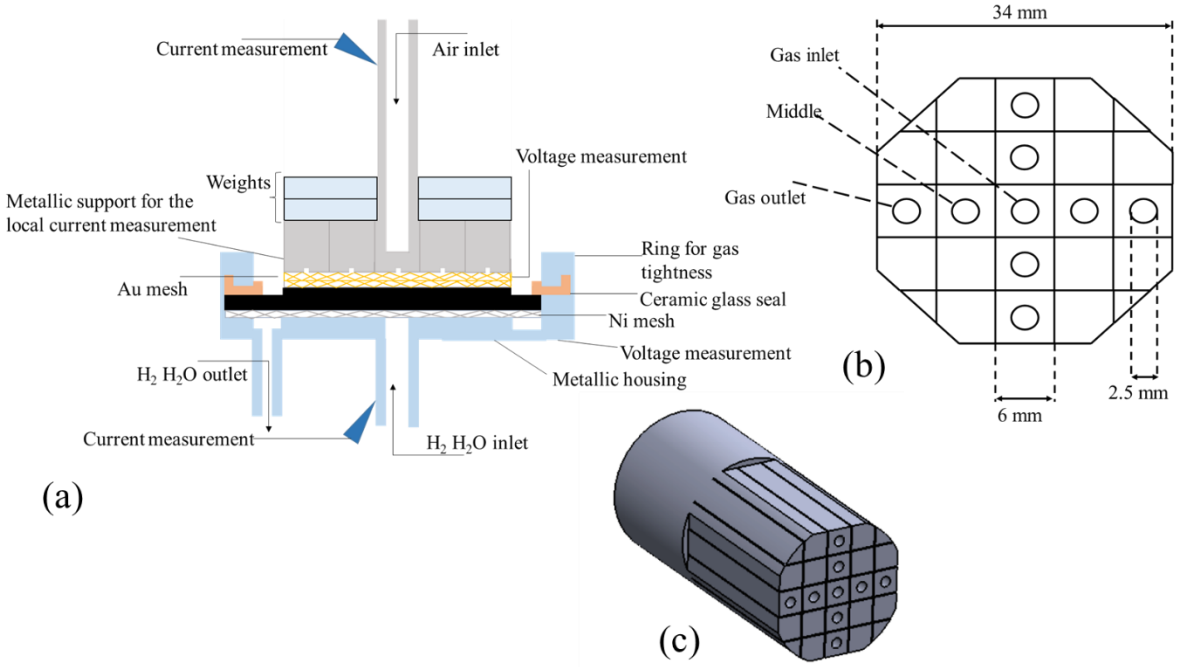

Figure 1 - Schematic illustration of (a) the testing setup, (b) cross-section and, (c) 3D view of the interconnect at the oxygen side for the local current measurements.

2.3 Protocol description

The experiment procedure started with the cell heating at a rate of 1 °C.min^{-1} up to 860 °C under a nitrogen and air sweeping at the fuel and air sides, respectively. Then, the cell was maintained at this temperature for 90 min to form the glass sealing. After, the temperature was lowered to 800 °C to start the cermet reduction. For this purpose, the hydrogen concentration at the inlet was increased gradually up to reach the full conversion of Nickel oxide into metallic Nickel.

Polarization curves were performed in fuel cell and electrolysis mode. For electrolysis mode, a ratio of $P(H_2)/P(H_2O)$ = 10/90 was used, whereas, in SOFC mode, the anode was supplied with dry hydrogen. In both cases, the air electrode was always supplied with synthetic air with

a constant flux of 41 $NmL.min^{-1}cm^{-2}$. The measurements were performed in galvanostatic mode (Autolab PGSTAT-302N) with a current rate of 21 $mA.s^{-1}$ and a 20 A current booster. The current local distribution was measured using a multichannel data logger HIOKI LR8400-20, able to record simultaneously the 9 voltage pins measurements. The data were acquired at different temperatures (700, 750 and, 800 °C) and for various inlet fluxes at the fuel electrode (3, 6, 9, and 12 $NmL.min^{-1}cm^{-2}$).

In order to assess the contact resistance (R_c) between the electrodes and the grids, electrochemical impedance spectroscopy has been also performed at the Open Circuit Voltage (OCV) for the three investigated temperatures (i.e. 700, 750 and, 800 °C and for an inlet flux at the fuel electrode of 12 $NmL.min^{-1}cm^{-2}$). The contact resistances have been calculated as a function of the temperature by removing the electrolyte ohmic resistance from the serial resistance measured on the impedance diagrams (i.e. high frequency intercept with the real axis in the Nyquist plot). The diagrams were also acquired in galvanostatic mode by imposing a sinusoidal current with an amplitude of 110 $mA.cm^{-2}$ in the frequency range of 10^{-2}-10^{4} Hz.

3. Model descriptions

3.1 General assumptions and multiscale model

A multiscale model was developed in order to unravel the complex relationships between the SOC response and the mechanisms that take place in the electrodes. This model is composed of three different length-scale modules that can achieve an exhaustive analysis of the cell performance in both SOEC and SOFC modes. The first module allows generating 3D digital twins of electrode microstructures made of classical materials. It can provide all the necessary morphological information for the other modules. The second module is a micro-scale model that takes into consideration the elementary reactions coupled with the mass and charge transfer in the active layer of both electrodes. Finally, the third module is a macro-scale model that can compute all the polarization curves and local current distribution along the cell radius.

The connections between the modules are established in different arrangements as it can be seen in Figure 2. The microstructural model provides all the morphologic inputs that are needed for the other modules. Moreover, the micro-scale modules provide the parameters of the ‘apparent’ or ‘global’ exchange current densities (i.e. activation energies and exponents - cf. Eqs. 4 and 5) for the calculation of the electrode activation overpotential in the macro-scale model. It can be noticed that the functional layers are not described at the macroscopic

scale. Therefore, the partial pressure distributions taken at the electrolyte interface in the macro-model are used in the micro-model as boundary conditions applied at the top of the functional layer. The model description at the microscopic scale must include a full description of the micro-processes involved in the reaction mechanism. In this approach, the parameters for the 'global' exchange current densities are identified in order to match with the electrode overpotential calculated in the active layer with the microscale models. Thanks to this method, all the processes in the functional layer are thus included in the apparent exchange current density of the Butler-Volmer equation for the macroscale model. In other words, it is possible to guarantee that the activation overpotentials in the macro-model take into consideration all microscopic processes arising in the electrode functional layers.

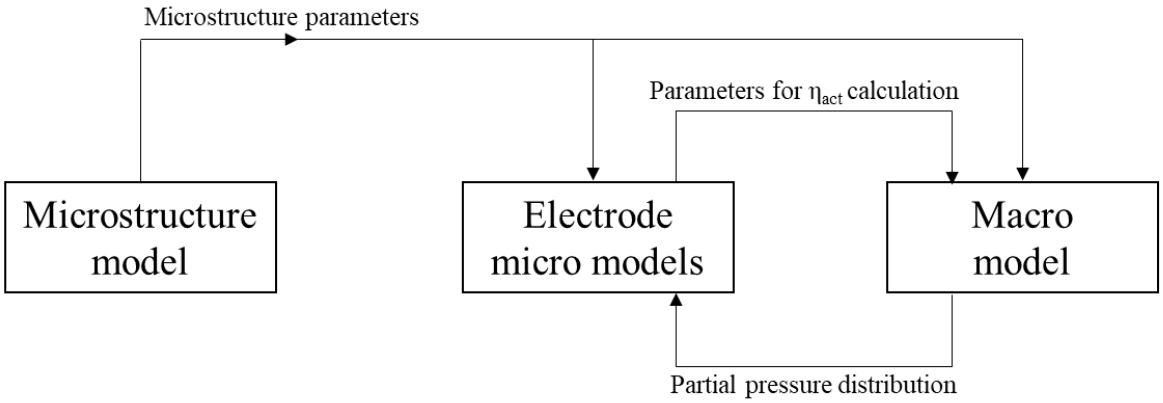

Figure 2 – General flowchart of the multiscale model

3.2 Microstructure model

To obtain digital twins of the real electrode structures, geostatistical simulations were carried out using a model based on a truncated plurigaussian random field method [24], [46]. In this method, each phase is represented by a random field, which is generated by the convolution of random noise with a weight function. Hence, the fields are jointly thresholded according to a specific procedure to obtain the synthetics microstructures [46]. This model was validated by comparison with 3D reconstructions of real electrodes performed by X-ray holotomography [27]. More details about the model and its validation can be found in [24]. In this work, we used the digital twins of the real electrodes as input for the electrochemical simulations.

3.3 Micro-scale models: electrodes functional layer

The micro-scale models are able to describe all the microscopic processes that take place in the active functional layer of both electrodes. These models are essential to understand the

role of the microstructure and the operating conditions (polarization, temperature, etc.) on the reaction mechanisms and electrode performances. Two models were developed considering the state-of-the-art materials with the LSCF-CGO [28], [47] composite and Ni-YSZ [48] cermet for the air and fuel electrodes, respectively. Both models were built up considering a slice of porous electrode described as a homogenous medium. A special attention was paid to describe the electrode kinetics in a sequence of elementary steps that can evolve in different reaction pathways depending on the polarization. The list of reactions implemented in the models are listed in Table 1 for both electrodes. All the kinetic constants are thermally activated and expressed with an Arrhenius law. Activations energies were already calculated and published in [28] and [48] for the air and fuel electrodes, respectively.

For the hydrogen electrode, the model is based on a hydrogen spillover mechanism proposed and validated in [49]. In this case, the reactions mechanism is co-limited by the charge transfer at Triple Phase Boundary lines (TPBls), the oxygen vacancies migration in the YSZ network and a pure chemical surface process depending on the polarization [48]. According to this model, steam can interact with the surface of both Ni and YSZ in two parallel pathways. Considering cathodic polarization (electrolysis mode), steam can adsorb on the Ni surface (cf. reaction R1 in Table 1), where it is reduced at the TPBls into one hydrogen adatom H_{Ni} attached on the Ni surface and one hydroxyl ions OH^-_{YSZ} on the YSZ surface (reaction R5). The hydroxyl ion OH^-_{YSZ} is then further reduced at the TPBls into a second hydrogen on the Ni surface and an oxygen ion O^{2-}_{YSZ} attached on the YSZ surface (reaction R6). Then, two hydrogens H_{Ni} can be associated and desorbed into H_2 molecules (reaction R4), while the oxygen ions O^{2-}_{YSZ} are incorporated into the YSZ lattice (reaction R7). In parallel, steam molecules can also adsorb on the YSZ surface (reaction R2). In this second pathway, the adsorbed water molecule can react with the oxygen ions available at the YSZ surface to produce hydroxyl ions OH^-_{YSZ} (reaction R3). As previously described, the hydroxyl ions can be reduced at TPBls according to reaction R6. It has been shown [50] that the first pathway (steam adsorption on Ni surface) is preferentially activated under electrolysis mode while the water desorption from YSZ (second pathway) is predominant in fuel cell mode. Nevertheless, the prevalence of one pathway should also depend on the local operating condition along the cell length that still need to be investigated.

Regarding the air electrode, the reaction mechanism proposed and validated in [28] is also divided into two parallel pathways. For an operation in electrolysis mode, the so-called bulk path starts by the ionic transfer reaction at the LSCF/CGO interface (reaction R8 in Table 1)

that supplies the electrode material in oxygen atoms $O^{x}_{O_{(LSCF)}}$. After a transport by solid-state diffusion in LSCF, the incorporated oxygen is released from the bulk to generate ad-ions $O^{-}_{(LSCF)}$ on the LSCF surface (reaction R9). For the second path, hereafter called surface path, the oxygens coming from the electrolyte material (i.e. CGO) are directly oxidized at the TPBls to produce oxygen ad-ions (reaction R10). Finally, the oxygen ad-ions are reduced in oxygen ad-atoms in a second reaction of charge transfer (reaction R11) which is common to the two pathways. The oxygen is then associated on the LSCF surface (reaction R12) before to be desorbed into the porosity (reaction R13). For a composite electrode, it has been shown that the surface path is dominant whatever the polarization even if the contribution of the bulk path is significantly enhanced in fuel cell mode [28]. As for the fuel electrode, the reaction mechanism is expected to change as a function of the local condition along the cell radius.

For both electrodes, mass and charge balances have been considered for all species. They constitute a set of partial differential equations that are implemented and solved using COMSOL Multiphysics®. Besides, all the equations for the transport and the kinetic rates are expressed as a function of the electrode microstructural properties. They are extracted from the digital twins obtained with the truncated random field, establishing a link between the two-length scales. Finally, it is worth noting that all the equations and the details for this module of the multiscale model have been already published in [48] and [28] for the fuel and the air electrodes, respectively. In these previous studies, a special attention was paid to validate the mechanisms using experimental results obtained on symmetrical cells tested in a three-electrode set-up.

Table 1 – Reactions and fitted values for the kinetic constants for T = 750 °C

Fuel electrode			
$H_2O_{(gas)} + 1s_{Ni} \underset{k^{ADS}_{H_2O_{Ni}}}{\overset{k^{DES}_{H_2O_{Ni}}}{\leftrightarrows}} H_2O_{Ni}$	Steam adsorption on the Ni surface (R1)	Ni interaction pathway	1.18 x 10^{6} (s^{-1})
$H_2O_{(gas)} + 1s_{YSZ} \underset{k^{ADS}_{H_2O_{YSZ}}}{\overset{k^{DES}_{H_2O_{YSZ}}}{\leftrightarrows}} H_2O_{YSZ}$	Steam adsorption on the YSZ surface (R2)	YSZ interaction pathway	9.28 x 10^{3} (s^{-1})
$H_2O_{YSZ} + O^{2-}_{YSZ} \underset{k^{DISS+}_{H_2O_{YSZ}}}{\overset{k^{DISS-}_{H_2O_{YSZ}}}{\leftrightarrows}} 2OH^{-}_{YSZ}$	H_2O dissociation on YSZ surface (R3)	YSZ interaction pathway	6.87 x 10^{16} ($m^2.s^{-1}.mol^{-1}$)
$2H_{Ni} \underset{k^{DES}_{H_2Ni}}{\overset{k^{ADS}_{H_2Ni}}{\leftrightarrows}} H_{2(gas)} + 2s_{Ni}$	Hydrogen desorption from Ni surface (R4)	Common pathway	3.69 x 10^{12} ($m^2.s^{-1}.mol^{-1}$)
$H_2O_{Ni} + 1s_{YSZ} + 1e^{-} \underset{k^{red}_{1}}{\overset{k^{ox}_{1}}{\leftrightarrows}} OH^{-}_{YSZ} + H_{Ni}$	First charge transfer reaction (R5)	Ni interaction pathway	8.5 x 10^{4} ($m^3.s^{-1}.mol^{-1}$)

$OH^-_{YSZ} + s_{Ni} + 1e^- \underset{k_1^{red}}{\overset{k_2^{ox}}{\leftrightarrows}} O^{2-}_{YSZ} + H_{Ni}$	Second change transfer reaction (R6)	Common pathway	5.5 x 10^5 ($m^3.s^{-1}.mol^{-1}$)
$O^{2-}_{YSZ} + V^{\bullet\bullet}_{(YSZ)} \underset{k^{EXC}_{O^{2-}_{YSZ}}}{\overset{k^{INC}_{O^{2-}_{YSZ}}}{\leftrightarrows}} O^x_{O(YSZ)} + s_{YSZ}$	Oxygen incorporation in the YSZ lattice (R7)	Common pathway	1.3 x 10^8 ($m^3.s^{-1}.mol^{-1}$)
Air electrode			
$O^x_{O(CGO)} + V^{\bullet\bullet}_{(LSCF)} \underset{k_+}{\overset{k_-}{\leftrightarrows}} O^x_{O(LSCF)} + V^{\bullet\bullet}_{(CGO)}$	Ionic transfer at LSCF/CGO interface (R8)	Bulk pathway	50 ($mol.m^{-2}.s^{-1}$)
$O^x_{O(LSCF)} + 1h^{\bullet} + 1s_{LSCF} \underset{k_{ox}^{LSCF/gas}}{\overset{k_{red}^{LSCF/gas}}{\leftrightarrows}} V^{\bullet\bullet}_{O(LSCF)} + O^-_{LSCF}$	Oxygen excorporation reaction (R9)	Bulk pathway	9 x 10^{-5} ($m^3.s^{-1}.mol^{-1}$)
$O^x_{O(CGO)} + 1h^{\bullet} + 1s_{LSCF} \underset{k_{ox}^{TPBls}}{\overset{k_{red}^{TPBls}}{\leftrightarrows}} V^{\bullet\bullet}_{O(CGO)} + O^-_{LSCF}$	Oxygen oxidation reaction at the TPBls (R10)	Surface pathway	2.25 x 10^{-4} (s^{-1})
$O^-_{LSCF} + 1h^{\bullet} \underset{k_{deion}}{\overset{k_{ion}}{\leftrightarrows}} O_{LSCF}$	Oxygen deionization reaction (R11)	Common pathway	8.74 x 10^5 (s^{-1})
$2O_{LSCF} \underset{k_{ass}}{\overset{k_{diss}}{\leftrightarrows}} O_{2LSCF} + 1s_{LSCF}$	Oxygen association reaction (R12)	Common pathway	1.5 x 10^{15} ($m^2.s^{-1}.mol^{-1}$)
$O_{2LSCF} \underset{k_{des}}{\overset{k_{ads}}{\leftrightarrows}} O_{2(gas)} + 1s_{LSCF}$	Oxygen desorption reaction (R13)	Common pathway	3.12 x 10^6 (s^{-1})

3.4 Macro-scale model: SRU and interconnects

In the macroscale model, the cell design and the geometry of the gas channels are taken into account considering a 2D approach as already detailed in [31], [32]. It couples locally fluidic and electrochemical steps, allowing the analysis of the distribution of gas composition and current density along the cell radius. In this macroscopic approach, the active functional layers are not described and they are limited to the electrode/electrolyte interface. The Dusty Gas Model (DGM), which takes into consideration the molecular and Knudsen diffusions, is used to describe the gas transport through the current collector in LSCF at the air side and the thick Ni-YSZ substrate at the hydrogen side. All the diffusion coefficients are calculated as a function of the microstructural properties [31], [32]. The main features of this macroscale model are briefly reminded hereafter.

Since the metallic interconnects present a very good electrical conductivity, the cell voltage (U_{cell}) is considered constant all along the cell length. In this way, Eq. 2 is applied to calculate the local current density along the cell radius *r*:

$$U_{cell} = E_{i=0} + \eta_{conc}^{O_2 electrode}(r) - \eta_{conc}^{H_2 electrode}(r) + \eta_{act}^{O_2 electrode}(r) - \eta_{act}^{H_2 electrode}(r) - \eta_{ohm}(r) \quad (2)$$

where $E_{i=0}$ is the Open Circuit Voltage (OCV), which is calculated by Nernst's equation. The terms η_{conc}, η_{act} and, η_{ohm} are the concentration, activation and, ohmic overpotential, respectively. Those terms increase the cell voltage in electrolysis conditions and decrease the cell voltage in fuel cell conditions. The ohmic overpotential includes (*i*) the contact resistances (R_C) arising between the electrodes and the interconnects, (*ii*) the ionic resistance of the electrolyte and (*iii*) the electronic resistances for the LSCF current collector and Ni-YSZ support.

The difficulty to maintain the gas composition at the active sites is taken into account in the concentration overpotential. This term is the sum of the gas diffusion overpotential (η_{diff}) and the gas conversion overpotential (η_{conv}). The first contribution is due to the losses ascribed to the gas transfer through the porous media (i.e. LSCF current collector and Ni-YSZ support described at this macroscale). The second contribution is related to the thermodynamic losses that are induced by the change in the gas composition due to the consumption or production of the gaseous species along the cell length. Finally, the activation overpotentials must take into account all the microscopic processes occurring in the Ni-YSZ and LSCF-CGO functional layers (i.e. all the reactions convoluted with the mass and charge transfers as described in the microscale models). For this purpose, they are calculated using a phenomenological Butler-Volmer equation as shown in Eq. 3.

$$\left|\eta_{act}^{O2\ electrode}\right|+\left|\eta_{act}^{H2\ electrode}\right|=\frac{RT}{F}sinh^{-1}\left\{\frac{|i(r)|}{2i_0^{O2\ electrode}(r)}\right\}+\frac{RT}{F}sinh^{-1}\left\{\frac{|i(r)|}{2i_0^{H2\ electrode}(r)}\right\} \quad (3)$$

The terms $i_0^{O2\ electrode}(r)$ and $i_0^{H2\ electrode}(r)$ are defined as the 'global' exchange current densities for each electrode. They are a function of the local partial pressure p_i taken at the electrode/electrolyte interface, as can be seen in Eqs. 4 and 5.

$$i_0^{H_2\ electrode}=\mathrm{A}\times\left(p_{H_2}(r)\right)^{\mathrm{m}}\times\left(p_{H_2O}(r)\right)^{\mathrm{n}}\times\mathrm{e}^{\left(-\frac{\mathrm{E_a}^{H_2 electrode}}{\mathrm{RT}}\right)} \quad (4)$$

$$\mathrm{i}_0^{O_2 electrode}=\mathrm{B}\times\left(p_{O_2}(r)\right)^{\mathrm{p}}\times\mathrm{e}^{\left(-\frac{\mathrm{E_a}^{O_2 electrode}}{\mathrm{RT}}\right)} \quad (5)$$

The parameters *m*, *n* and, *p* denote the exponent on the partial pressures dependency whereas $\mathrm{E_a}^{O_2 electrode}$ and $\mathrm{E_a}^{H_2 electrode}$ are the activation energy for the oxygen and hydrogen electrodes, respectively. The computation of these parameters is carried out using the

microscale model as detailed in section 3.1, in such a way that the macroscale model takes into account all the electrochemical phenomena occurring in the electrode functional layers.

4. Results

4.1 Microstructural modeling

The digital twins of the LSCF current collector and the LSCF-CGO and Ni-YSZ functional layers are compared in Fig. 3 and 4 to the reconstructions of the real electrodes obtained by FIB-SEM (Focused Ion Beam-Scanning Electron Microscopy) tomography according to the protocol already published in [27]. As expected, it can be observed that the synthetic microstructures seem to mimic accurately the real ones. As a verification, the microstructural properties listed in Table 2 have been calculated on both types of volume using the numerical procedures thoroughly detailed in [24]. The computations have been carried out on volumes as large as 15^3 μm^3, which can be considered as a Representative Volume Element (RVE) for this type of microstructures [24]. Whatever the studied layer, a good match has been found between the two sets of data. For instance, the mean error between the parameters computed on the real and synthetic microstructures for the LSCF-CGO does not exceed 10%. Moreover, it has been also checked that the mean error for the LSCF and Ni-YSZ microstructures lies in the range of a few percent. Therefore, these results validate the generation of synthetic microstructures for the standard cell tested in this work.

The Ni-YSZ support has been reconstructed by synchrotron X-ray tomography according to procedure given in [50]. As shown in Fig. 4, this technique allows obtaining a large reconstructed volume, required to be representative of this coarse microstructure [51]. The microstructural properties for the support have been computed on several sub-volumes extracted from the whole reconstruction [51]. Knowing that the standard deviation on the data is very small, only the mean value for the parameters is given in Table 2. It can be noticed in Fig. 4 that the porosity of the support exhibits a large pore size distribution. This particular feature is explained by the utilization of pore former during the manufacturing. Because of this characteristic, the truncated random field method fails to reproduce correctly the microstructure. In this case, models based on sphere packing are more adapted to reproduce microstructures exhibiting a multi-modal distribution of pore size [51].

Finally, it is worth noting that all the data given in Table 2 provide a complete description of the electrode microstructures, which are necessary for the electrochemical simulations described hereafter.

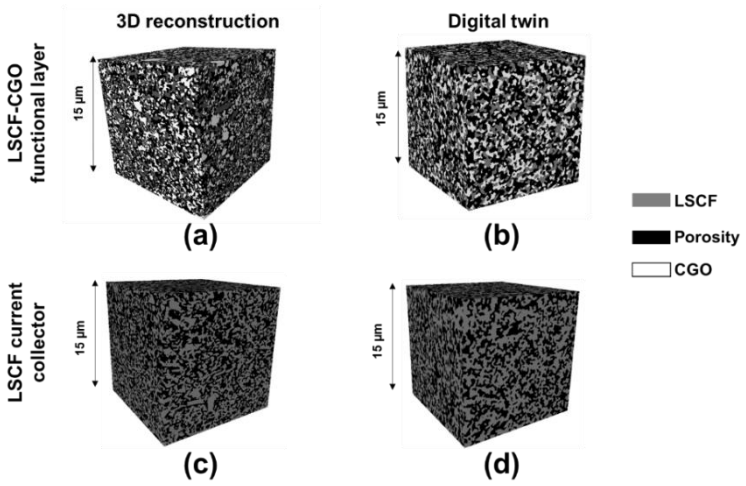

Figure 3 – Comparison between the microstructures of the LSCF-CGO functional layer obtained by 3D reconstruction (a) and by the microstructural modeling (b); and for the LSCF current collector microstructures obtained by 3D reconstruction (c) and by the microstructural modeling (d).

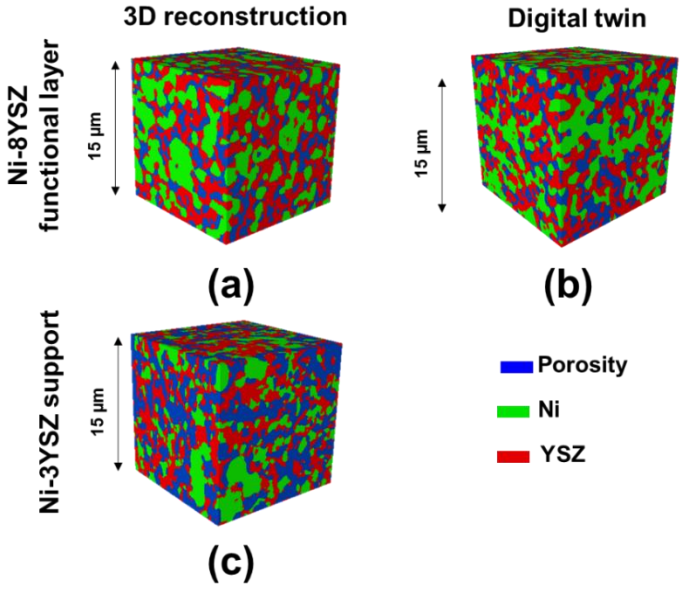

Figure 4 – Comparison between the microstructures of the Ni-8YSZ functional layer obtained by 3D reconstruction (a) and by the microstructural modeling (b) and a 3D reconstruction of the Ni-3YSZ support (c).

Table 2 – Microstructure properties of the fuel and air electrodes

Properties of the connected phases	**Ni-8YSZ functional layer**	**Ni-3YSZ support**	
Pores volume fraction (ε_{pores})	0.234	0.39	(%)
Nickel volume fraction (ε_{Ni})	0.329	0.26	(%)
YSZ volume fraction (ε_{YSZ})	0.425	0.35	(%)
Specific surface area between YSZ and pores ($Sp_{YSZ-pores}$)	1.49	1.44	(μm^{-1})
Specific surface area between pores and Ni ($Sp_{pores-Ni}$)	0.343	0.60	(μm^{-1})
Specific surface area between Ni and 8YSZ (Sp_{Ni-YSZ})	0.984	1.38	(μm^{-1})
Mean pore radius ($\bar{r}_{pore}$)	0.14	0.325	(µm)
Pores tortuosity factor (τ_{pore})	5.3	3.74	(-)
Ni tortuosity factor (τ_{Ni})	6.5	8.88	(-)
YSZ tortuosity factor (τ_{YSZ})	2.45	3.53	(-)
Triple phase boundary length density (ξ_{TPB})	3.15	-	(μm^{-2})
Properties of the connected phases	**LSCF-CGO functional layer**	**LSCF current collector**	
Pores volume fraction (ε_{pores})	0.459	0.476	(%)
LSCF volume fraction (ε_{LSCF})	0.263	0.524	(%)
CGO volume fraction (ε_{CGO})	0.254	-	(%)
Specific surface area between LSCF and pores ($Sp_{LSCF-gas}$)	2.61	6.09	(μm^{-1})
Specific surface area between LSCF and CGO ($Sp_{LSCF-CGO}$)	1.05	-	(μm^{-1})
Mean pore radius ($\bar{r}_{pore}$)	0.068	0.074	(µm)
Triple phase boundary length density (ξ_{TPB})	17.81	-	(μm^{-2})
Pores tortuosity factor (τ_{pore})	1.89	1.86	(-)
LSCF tortuosity factor (τ_{LSCF})	9.5	2.27	(-)
CGO tortuosity factor (τ_{CGO})	13.15	-	(-)

4.2 Model calibration

The calibration of the multiscale model was performed in order to match the activation overpotentials calculated at the cell level and the overpotentials induced by all the processes in the active functional layers. To achieve this goal, the following procedure has been applied for both electrodes operated in SOFC and SOEC modes:

• First, the kinetic constants for the reactions implemented in the validated microscale models have been scaled up to reach the performances required at the cell level, using the polarization resistance measured by EIS at OCV and 750 °C as reference. This step consisted to multiply all the kinetic constants, previously determined on symmetrical cells [28], [48], by a correcting factor. Indeed, this correction is necessary since the electrode performances measured in a symmetrical setup are usually lower than those determined for the complete cell. Nevertheless, it is worth mentioning that neither the activation energies nor the reaction mechanism has been changed by this procedure. The values of the calibrated kinetic constants for the studied cell are given in Table 1 for both electrodes, considering electrolysis mode.

• The microscale models were then used to generate a large database of electrode polarization curves as function of the operating temperature and the gas partial pressures taken at the top of the active layers. To build this database, simulations were carried out by increasing the temperature from 700°C to 800°C. Furthermore, the partial pressures were changed from $P(H_2)/P(H_2O)$=10/90 to 90/10 for the fuel electrode and from $P(O_2)/P(N_2)$=10/90 to 100/0 for the air electrode.

• The parameters for the 'global' exchange current densities given by Eqs. (4) and (5) have been finally obtained by adjusting the activation overpotentials given by Eq (3) on the database related to the electrode polarization curves established for the active functional layers.

The fitted partial pressure exponents (*m* and *n* for the hydrogen side and *p* for the air side) and activation energy of the exchange current density are provided in Table 3 for both electrodes in SOFC and SOEC modes. For the hydrogen side, it can be noted that the steam presents a stronger impact than the hydrogen on the current exchange density. Similar results have been published in [52] and [53] with exponents m=0.11 and n=0.67 for SOFC polarization. For the air electrode, the value of the exponent is also consistent with the literature. For instance, exponents of 0.25 [52] and 0.26 [54] have been reported for the SOFC and SOEC modes, respectively. For the fuel electrode, the fitted activation energies are also consistent with the ones given in [55] and [56], with values of 100 $kJ.mol^{-1}$ and 140 $kJ.mol^{-1}$ in SOFC and SOEC modes, respectively. Finally, for the air electrode, the activation energies reported in [54] (83 $kJ.mol^{-1}$) and in [55] (120 $kJ.mol^{-1}$) for SOEC and SOFC modes, respectively, are in relative good agreement with the fitted values.

In this procedure for the model calibration, it is worth noting that the contact resistances deduced from the experimental impedance spectra have been introduced as inputs data in the simulations. As expected, R_C values have been found to decrease with the temperature [57]

(values of 0.244 Ω.cm², 0.181 Ω.cm², and 0.131 Ω.cm² were measured for 700 °C, 750 °C and 800 °C, respectively).

Table 3 – Parameters for exchange current densities

		Partial pressure exponent	Activation energy (kJ mol^{-1})	Pre-exponential factors
SOFC	H_2 electrode	m = 0.06 and n = 0.48	100	A=1.26x10^9 (A.m^{-2}.atm$^{-(m+n)}$)
	O_2 electrode	p = 0.21	112	B=8.12x10^9 (A.m^{-2}.atm^{-p})
SOEC	H_2 electrode	m = 0.10 and n = 0.80	130	A=2.63x10^{10} (A.m^{-2}.atm$^{-(m+n)}$)
	O_2 electrode	p = 0.16	88	B=1.1x10^{12} (A.m^{-2}.atm^{-p})

4.3 Model validation

The polarization curves of the complete cell have been measured in SOEC ($P(H_2)/P(H_2O)$ = 10/90) and SOFC ($P(H_2)/P(H_2O)$ = 100/0) modes for different fluxes introduced at the inlet of the fuel electrode (Figs. 5a and 5b) and for different temperatures (Fig. 5c and 5d). As a general matter, the experimental results are found to be coherent with the ones expected for this type of cell [3], [32]. It can be noticed that the OCV values are in excellent agreement to the theoretical values given by the Nernst equation (considering $P(H_2)/P(H_2O)$ = 10/90 for SOEC and $P(H_2)/P(H_2O)$ > 99/1 for SOFC mode). Moreover, the OCV values remained constant when changing the total inlet flux for the fuel electrode during the experiments. These statements point out that there was no significant leakage between the electrode compartments so that the gas tightness of the glass seal was considered satisfactory.

As expected, the cell presents higher performances when the operating temperature and the gas inlet flux at the hydrogen side are increased. For instance, at the thermo-neutral voltage (≈1.3 V [58]) in SOEC mode, the absolute value of the current density at 750 °C is increased from -0.39 A.cm^{-2} to -1.05 A.cm^{-2} when the inlet flux is increased from 3 NmL.min^{-1}cm^{-2} to 12 NmL.min^{-1}cm^{-2} (Fig. 5a).

The comparison between the experimental and simulated polarization curves is also provided in Fig. 5. It can be seen that the model is able to predict all the experimental data in both SOFC and SOEC polarizations without any type of fitting. Therefore, the model can reproduce accurately the effect of temperature and inlet flux on the cell performance.

Nonetheless, a minor difference between the shape of the simulated and experimental curves can be observed in the region of the cell limiting current density. This slight discrepancy must be probably ascribed to small uncertainties in the determination of the microstructural properties on the 3D reconstruction on the cell support (i.e. pore radius and tortuosity factor). Indeed, as they control the mass transfer across the tick substrate, even a small change of one of these parameters can affect significantly the diffusion process, which can increase the concentration overpotential and decrease the cell performances [32], [59].

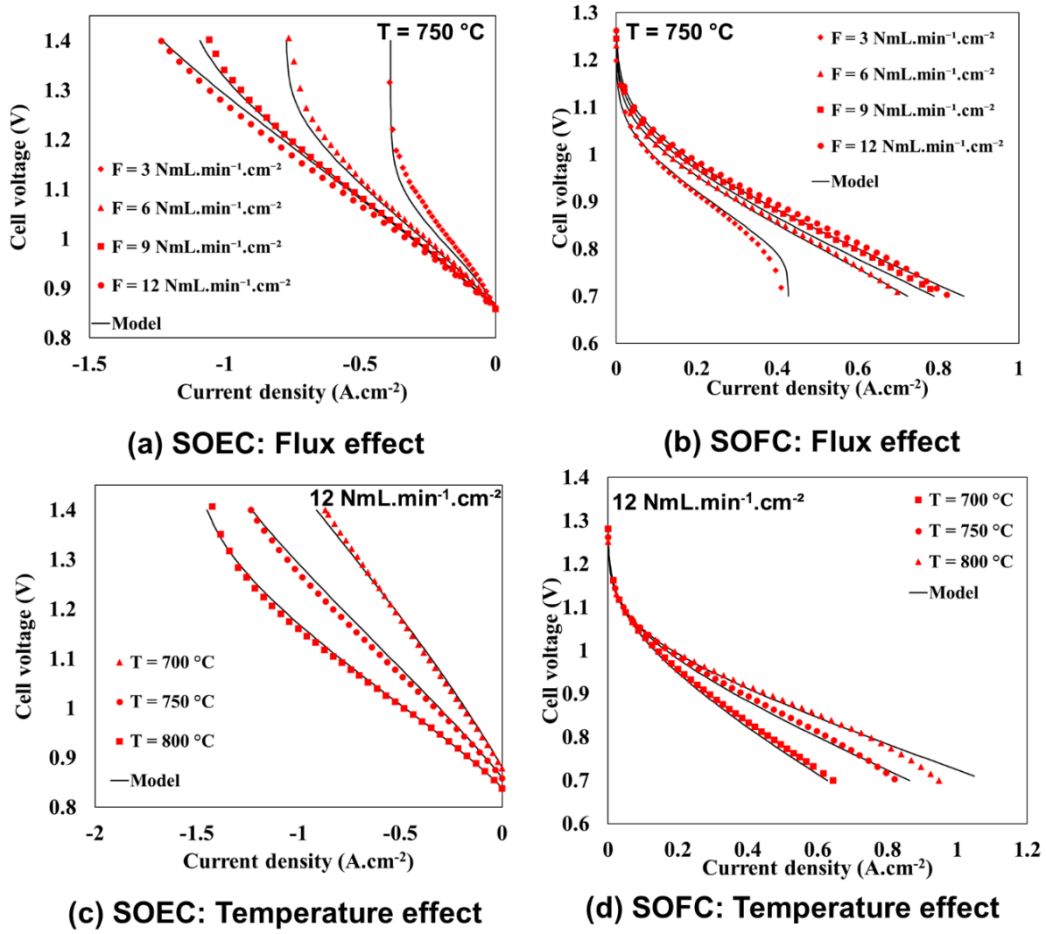

Figure 5 – Polarization curves showing the effect of the inlet gas flux at 750 °C in (a) SOEC and (b) SOFC modes, and effect of the temperature for a flux of 12 NmL.min^{-1}.cm^{-2} at 750 °C in (c) SOEC and (d) SOFC modes.

To go deeper in the model validation, the local polarization curves have been measured with our specific setup at the cell inlet, middle and outlet. The results obtained in SOEC modes are compared in Figs. 6a-6c to the local polarization curves extracted from the simulations in the same operating conditions than the experiments. It can be noted that the cell response is

strongly heterogeneous along the electrode radius, the performances decrease continuously from the gas inlet (cell center) up to the outlet (cell periphery). Moreover, it can be observed that this evolution of the local polarization curves is enhanced when the temperature is increased. This heterogeneity along the electrode radius is mainly induced by the loss in performance caused by the steam consumption and depletion from the inlet to the outlet [17], [41]. Indeed, the strong gradient in steam partial pressure along the cell radius (cf. Fig. 8) increases the local concentration overpotentials, which in turn lead to decrease the local current densities. In the most critical condition (i.e. T = 800 °C, curve related to the edge position), it becomes possible to observe the beginning of a turning back behavior of the curves as shown in Fig. 6c. This phenomenon was already reported by [17], using a segmented electrode in SOFC operations. It is related to the local current density distribution in the cell and its evolution with the polarization. At low polarization, the repartition of the current is quite homogeneous all along the cell length. In this condition, the local current densities increase with the polarization even in the cell outlet. However, the gradient becomes more and more pronounced with the polarization, due to the fuel shortage (or starvation) close to the cell outlet (i.e. at high fuel utilization in SOFC mode or steam conversion in SOEC mode). Therefore, after increasing, the local current density at the cell outlet starts to decrease. This 'bell-shaped' evolution for the local current density at the cell outlet explains the turning-back behavior in the local cell polarization at the cell outlet.

It is worth mentioning that a very good agreement is found between the experimental data and simulations for all the investigated conditions in Figs. 6a-6c. The model is thus able to predict the heterogeneity along the electrode radius measured in SOEC mode. Moreover, the simulations reproduce correctly the shape of the curves changing with the temperature. For instance, the turning back behavior highlighted at 800°C is well caught by the model.

The same analysis has also been conducted in SOFC mode at 750 °C and 800°C (Figs. 6d and 6e). As stated for the SOEC mode, the comparison between the experimental data and the computations also confirms that the model simulates quite precisely the evolution of the local polarization curves along the cell radius in SOFC mode. As expected, the local cell performances are decreased from the inlet to the outlet due to the consumption of hydrogen.

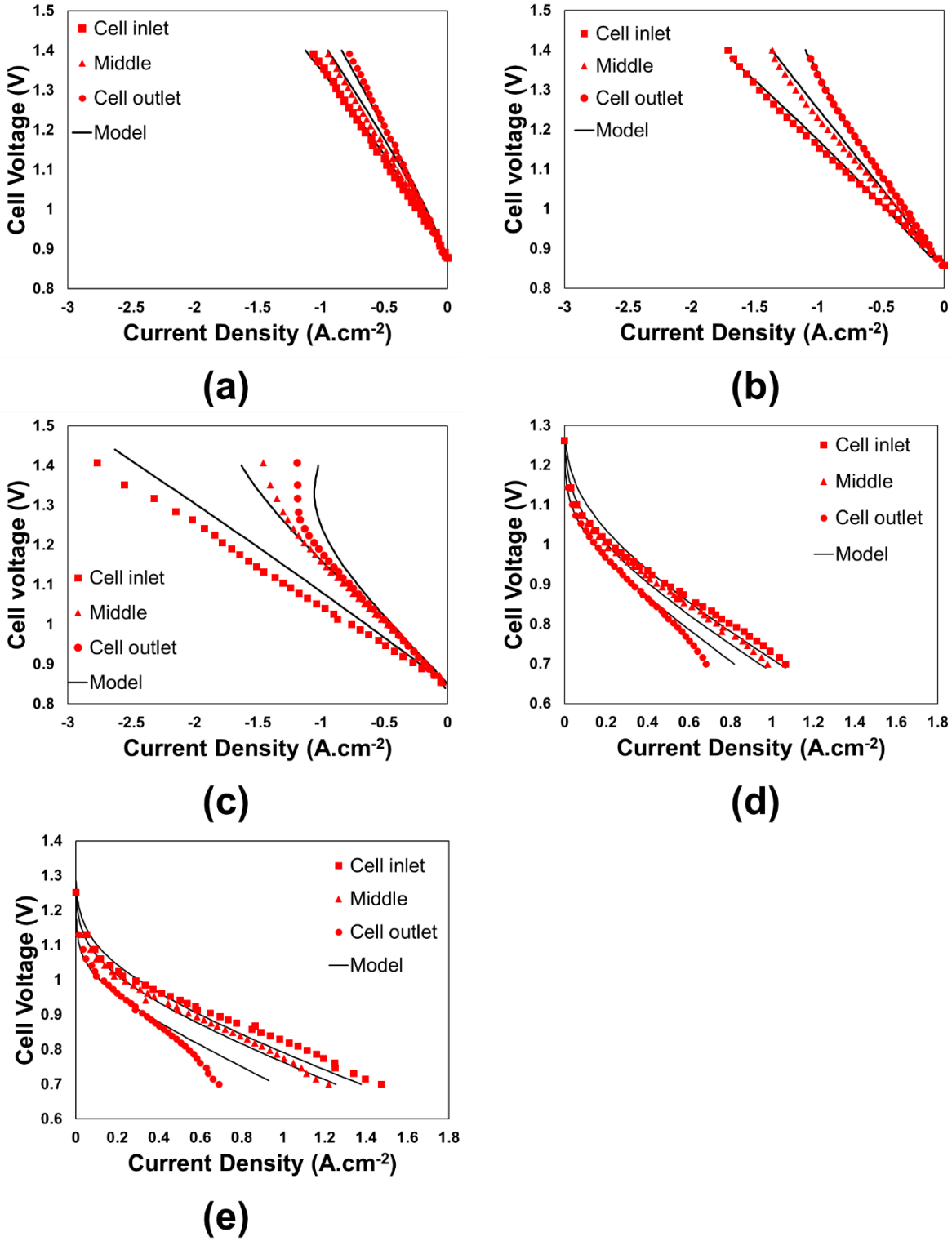

Figure 6 – Local polarization curves of cell inlet, middle and outlet for a flux of 12 $NmL.min^{-1}.cm^{-2}$ in SOEC mode at (a) 700 °C, (b) 750 °C and (c) 800 °C and in SOFC mode at 750°C (d) and 800 °C (e).

In Figs. 7a-7c, the local current densities have been plotted as function of the position along the electrode radius in SOEC mode at 700 °C, 750 °C, and 800 °C. Different conditions of cell voltage were chosen for the analysis: one in the region of higher current densities at 1.3 V and the other for an intermediate polarization at 1 V. The experimental data are represented by the red and blue segments, which are related to the local current density measured in each pin at 1.3 and 1 V, respectively. In all situations, the current density profile decreases from the gas inlet in the direction of the cell periphery. This behavior, which is more pronounced at higher temperatures and cell voltage, is in perfect line with the evolution of the local polarization curves. Indeed, as already explained, this evolution of the current density along the cell radius is due to the consumption of steam, which is favored at higher temperatures and higher cell voltages. With this representation, it can be seen that the computed currents along the cell radius are fully consistent with the measurements. Indeed, the simulated curves cross all the segments except at the cell inlet were experimental data are slightly above the predicted currents. This slight discrepancy could be explained by the contact resistances between the grids and the electrodes, which could not be perfectly homogenous in the experiments. It is thus proposed that the contact resistance below the pin at the cell inlet would be slightly lower in such a way that the current density would be higher (and hence, the simulated current systematically lower). Finally, it is worth noting that the same behavior is observed in SOFC mode under polarization at 0.8 V and 1 V at 750 °C and 800 °C (Figs. 7d and 7e).

As a general mater, when analyzing the global polarization curves in Fig. 5 together with the local results shown in Figs. 6 and 7, it is possible to conclude that the multiscale model is validated with the global and local measurements obtained for various operating conditions. Moreover, it has been shown that the experimental data obtained using the special setup is consistent with the expected results for this type of cell. Hence, it is possible to state that there is a mutual validation between the experimental data and the multiscale model. In other words, the general good agreement between the modeling results and the experimental data can be seen as a cross validation of the model with our specific setup proposed to measure the local polarization curves.

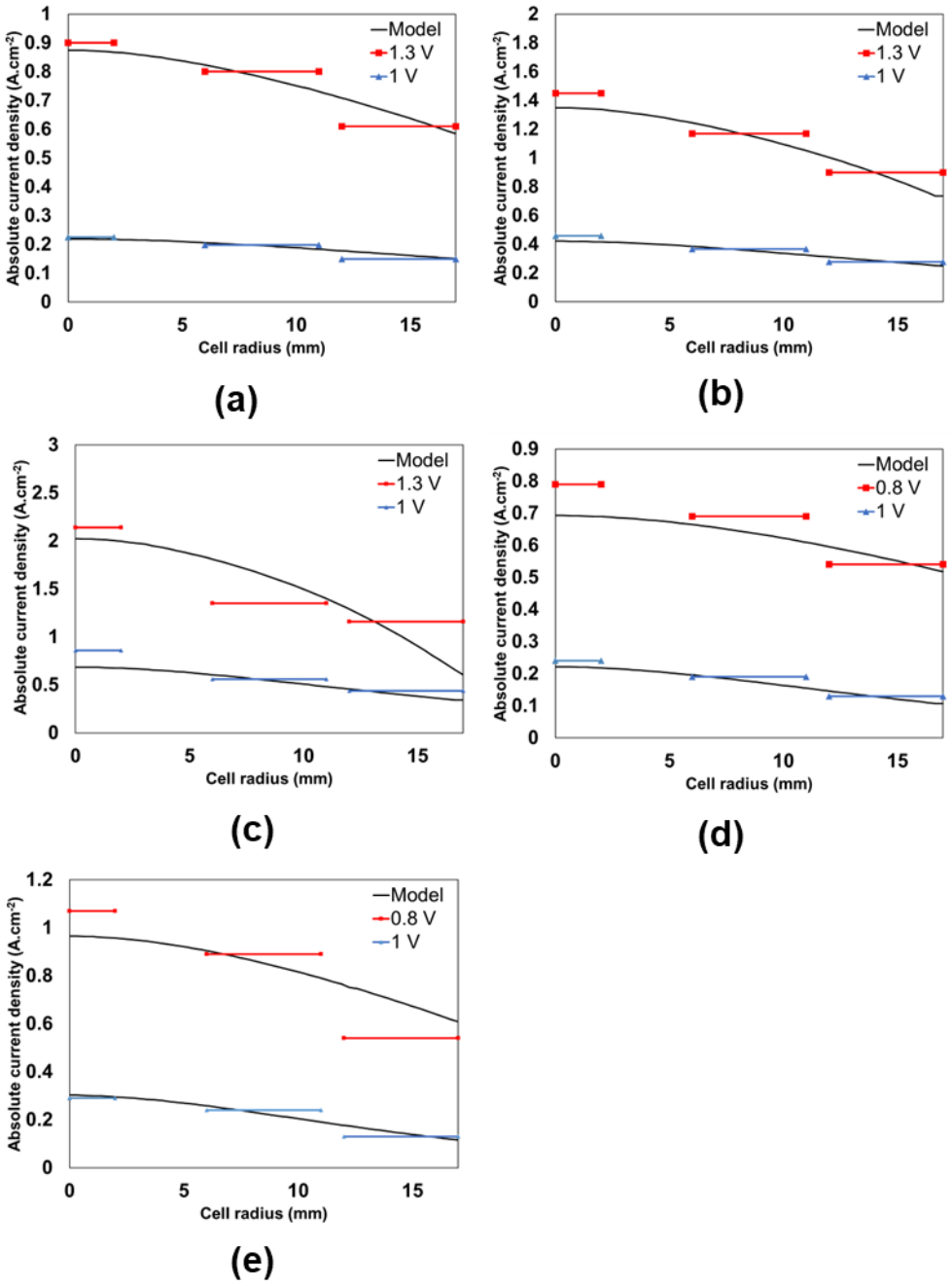

Figure 7 – Radial distribution of the current in SOEC mode (cell voltage of 1.3 V and 1 V, inlet flux = 12 NmL.min^{-1}cm^{-2}, P(H_2)/P(H_2O) = 10/90) at (a) 700 °C, (b) 750 °C and (c) 800 °C and in SOFC mode (cell voltage of 0.8 V and 1 V, inlet flux = 12 NmL.min^{-1}cm^{-2}, P(H_2)/P(H_2O) = 100/0) at (d) 750 °C and (e) 800°C.

5. Discussion

5.1 Partial pressures distribution

The multiscale model offers the possibility to compute all the quantities in the electrodes such as the radial distribution of the partial pressure under different conditions of inlet flux, polarization and temperature. As an illustration, the steam and hydrogen partial pressures have been plotted in Figs. 8a and 8b at the interface between the electrolyte and the fuel electrode. These distributions have been determined at 750 °C for a current density of ± 0.5 $A.cm^{-2}$ in both SOEC ($P(H_2)/P(H_2O)$ = 10/90) and SOFC modes ($P(H_2)/P(H_2O)$ = 90/10) and for two different inlet fluxes (6 and 12 $NmL.min^{-1}.cm^{-2}$). As expected, in SOEC mode, hydrogen partial pressure increases in the direction of the cell outlet, while the steam partial pressure decreases, since they are respectively produced and consumed by the electrochemical reactions. In SOFC mode, the partial pressures distribution follows an opposite evolution with a decrease of hydrogen concentration and an increase of steam concentration at the cell outlet.

The effect of the inlet flux for the fuel electrode is also shown in Figs. 8a and 8b. When the steam and hydrogen supply is lowered, the depletion of reactants in both modes is higher for a given current density. In that condition, the gradients along the cell radius are more pronounced as shown in Fig. 8a and 8b. At high fuel utilization in SOFC mode, the starvation of hydrogen at the cell outlet can accelerate the processes of cermet degradation with the local Ni re-oxidation into NiO [60].

The distributions of the oxygen and nitrogen partial pressures in the air electrode are also shown in Fig. 8c and 8d. It can be noticed that the gradients of partial pressures along the cell radius are not strongly affected by the cell operation in both modes. These slight evolutions are explained by the high inlet flux of air (41 $NmL.\ min^{-1}.cm^{-2}$) that guarantees a supply of oxygen all along the electrode radius.

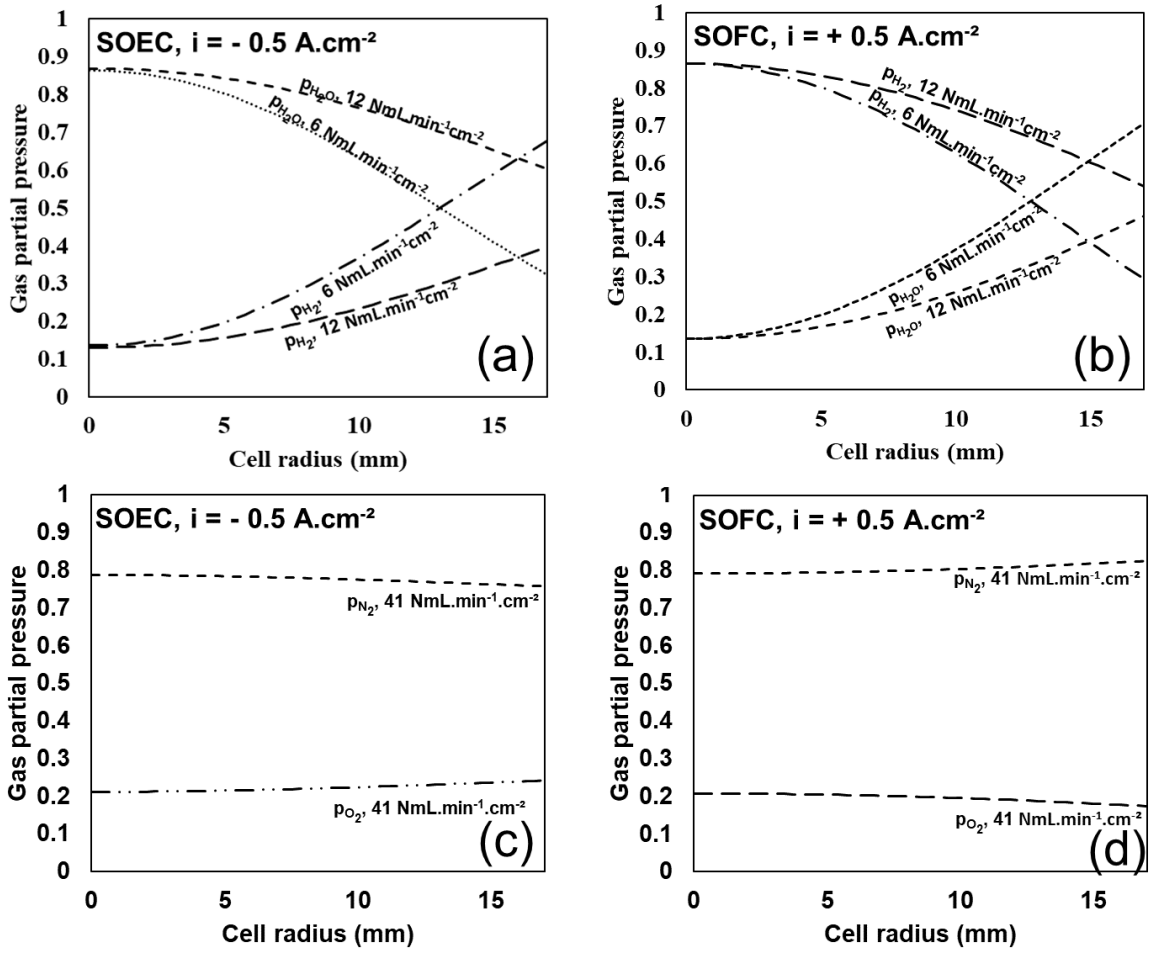

Figure 8 – Partial pressures of H_2 and H_2O along the cell radius for 6 NmL.min^{-1}cm^{-2} and 12 NmL.min^{-1}cm^{-2} at 750 °C under (a) cathodic polarization and partial pressure in the gas inlet of $P(H_2)/P(H_2O)$ = 10/90, and (b) anodic polarization and partial pressure in gas inlet of $P(H_2)/P(H_2O)$= 90/10. Partial pressures of O_2 and N_2 along the cell radius for 41 NmL.min^{-1}cm^{-2} at 750 °C under (c) anodic polarization and partial pressure in the gas inlet of $P(O_2)/P(N_2)$ = 21/79, and (d) cathodic polarization and partial pressure in the gas inlet of $P(O_2)/P(N_2)$ = 21/79.

5.2 Reaction mechanism in the fuel electrode

The extent of the active reaction zone in the fuel electrode can be quantified by plotting as a function of the electrode thickness the local ionic (i_{io}) and electronic (i_{el}) current densities in YSZ and Ni [61]. These evolutions have been extracted from the simulating results for the three positions along the electrode radius at the cell inlet, middle and outlet. They are reported in Fig. 9 for a cell operating at 750°C and ±0.5 A.cm^{-2} in SOFC and SOEC mode. As expected, the electronic current density increases from the electrolyte interface up to the current collector while the ionic current density follows the opposite evolution. With the

studied microstructure, it can be noticed that the reactions spread over a distance of around 15 µm in the cermet thickness when operated in electrolysis mode (Fig. 9a). Moreover, it is found that the repartition of the current density in the active layer is not significantly impacted by the position along the cell radius. From a practical point of view, this statement means that it is not necessary to tune the thickness of the functional layer from the cell inlet to the outlet during manufacturing. Finally, it can be noticed that the same statement has been found when the cell is operated in fuel cell mode (Fig. 9b). Nevertheless, the extension of the reaction zone in the electrode is slightly lower than in SOEC mode. This difference is related to a change in the activated reaction mechanism, which is detailed hereafter.

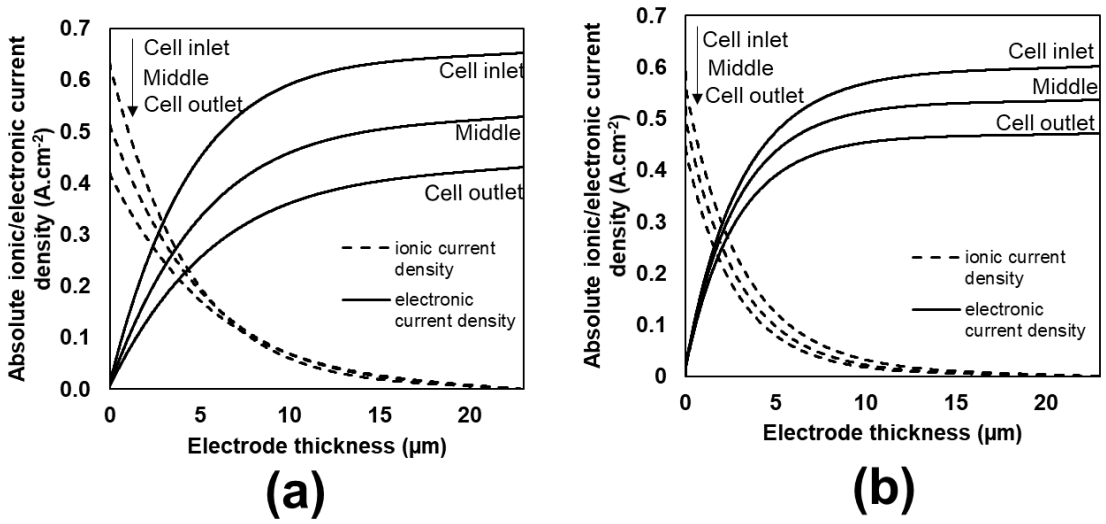

Figure 9 – Distribution of the ionic and electronic currents along the electrode thickness for different radial positions with an inlet gas flux of 12 NmL.min^{-1}.cm^{-2}, T = 750 °C and P(H_2)/P(H_2O) = 50/50 in (a) SOEC mode at -0.5 A.cm^{-2} and (b) SOFC mode at +0.5 A.cm^{-2}.

To highlight the effect of the position on the reaction mechanism, the ratio (ξ) between the kinetic rates of steam adsorption/desorption on YSZ (v_{R2}) and Ni (v_{R1}) (cf. Table 1) has been computed at the cell inlet, middle and outlet:

$$\xi(r) = \frac{\int_{z=0}^{z=FL} v_{R2}(z,r)\,dz}{\int_{z=0}^{z=FL} v_{R1}(z,r)\,dz} \quad (6)$$

A ratio higher than one means that the mechanism is mainly controlled by the reaction pathway related to the steam interaction with YSZ. On the contrary, a ratio lower than one

indicates that reaction mechanism is dominated by the pathway related to the steam interaction with Ni.

This ratio is plotted in Fig. 10a for an operation in SOFC mode at 750°C and i=+ 0.5 A.cm^{-2}. As already explained in [48], the majority of the steam is produced in fuel cell mode by the water desorption from the YSZ surface (ξ>1). Nevertheless, the ratio between the two pathways decreases in the direction of the cell outlet. This evolution in the reaction mechanism along the cell radius can be explained by the inspection of the surface coverages on the Ni and YSZ (Fig. 11). For the water molecules, it can be remarked that both coverages on Ni and YSZ increases from the inlet up to the outlet (Fig. 11a and 11b) since the steam partial pressure is higher at the cell periphery (Fig. 8b). However, it is worth noting that the increase of Θ_{H_2O} at the cell outlet is stronger for the Ni surface than for the YSZ. Indeed, an increase of 4.5x is found for Ni surface between the inlet and outlet (Fig. 11a), whereas in the same conditions, an increase of 2.3x is found for the local coverage on YSZ surface (Fig. 11b). This evolution points out that, compared to the cell inlet, the capability of the YSZ surface at the cell outlet to accept additional water molecules becomes limited. This trend is related to the very high coverage of hydroxyl ions resulting in low available sites on the YSZ surface when the steam partial pressure is increased (Fig. 11c and Fig. 11d). On the other hand, the available site on Ni tends to increase at the cell outlet due to the decrease of hydrogen ad-atom surface concentration (Fig. 11e and Fig. 11f). As a result, the reaction pathway with the steam desorption from YSZ becomes more and more bounded in the direction of the cell outlet while the one from Ni surface becomes favored. Finally, it can be noticed that the decrease of the ratio along the cell radius is enhanced when the inlet gas flux is lowered (Fig. 10a). Indeed, the higher fuel utilization leads to a stronger gradient of gas partial pressure along the electrode radius, and hence, a higher steam partial pressure at the cell outlet (cf. Fig. 8b).

Regarding an operation in SOEC mode, the ratio has been computed along the cell radius at 750°C and i=-0.5 A.cm^{-2} (Fig. 10b). It can be noted that the ratio follows an opposite behavior when compared to the SOFC mode. Indeed, it increases in the direction of the cell outlet, changing the prevailing mechanism of interaction between steam molecules and the electrode surface. At the cell inlet, the mechanism is mainly controlled by the adsorption of steam on Ni surface (i.e. ξ<1) while, at the cell outlet, the mechanism becomes more and more dominated by the steam adsorption on YSZ (i.e. ξ>1). As for the SOFC mode, this behavior can also be explained by analyzing the distribution of surface coverages on YSZ and

Ni. For instance, the evolution of Θ_{H_2O} along the cell radius is shown in Fig 12a and 12b on both materials. A decrease of 60% is found for the surface coverage on Ni from the inlet to the outlet. On the other hand, the decrease in the steam coverage is only about 35% for YSZ. Hence, the quantity of steam associated with the YSZ surface increases as a function of the electrode radius, which favors the reaction pathway that takes into consideration the adsorption on the YSZ surface, increasing the ratio ξ.

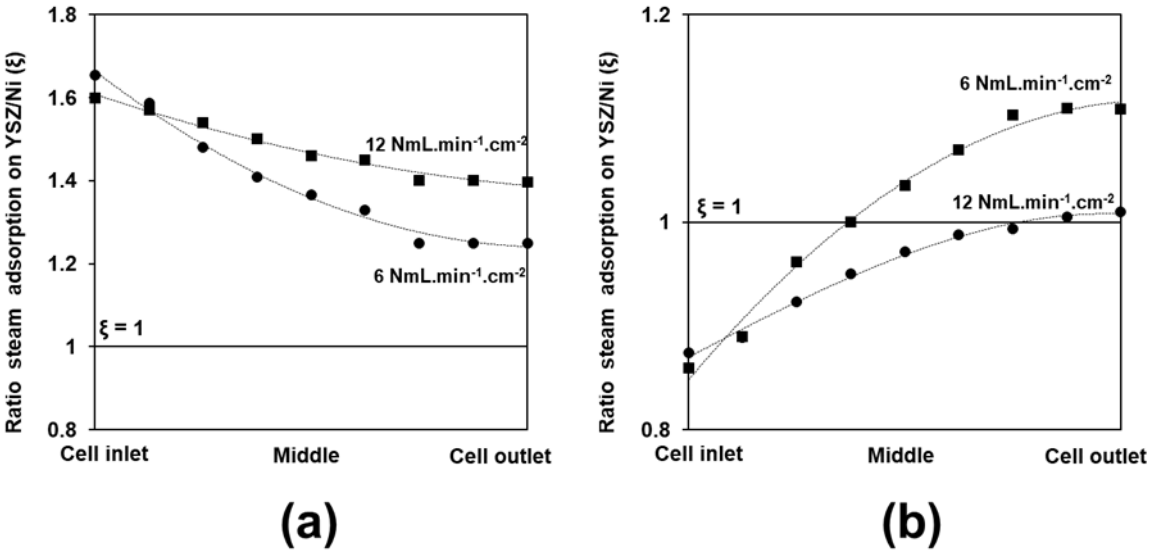

Figure 10 – (a) Ratio between the kinetic rates of steam desorption on Ni and YSZ surfaces as a function of the cell radius at 750 °C, with an inlet gas flux of 6 NmL.min^{-1}.cm^{-2} and 12 NmL.min^{-1}.cm^{-2} in (a) SOFC mode ($P(H_2)/P(H_2O)$ = 90/10) at i = +0.5 A.cm^{-2}, and (b) SOEC mode ($P(H_2)/P(H_2O)$ = 10/90) at i = -0.5 A.cm^{-2}.

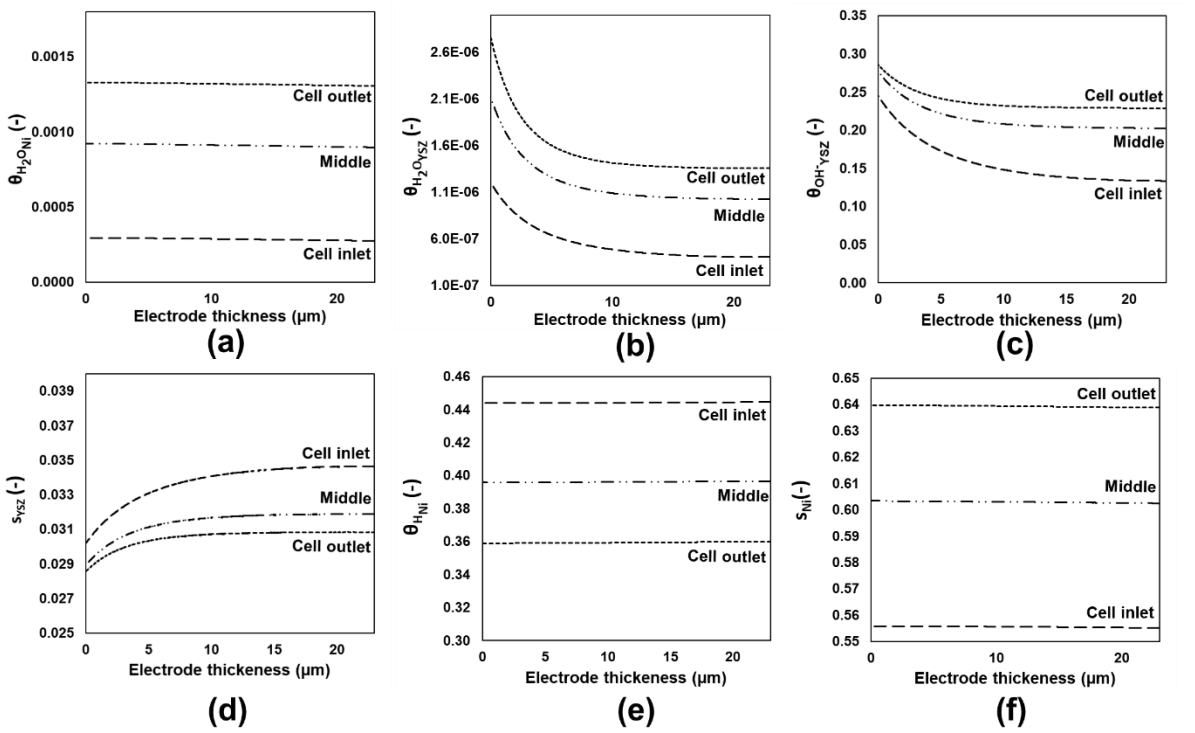

Figure 11 – Evolution of the surface coverage on YSZ and Ni surfaces in SOFC mode ($P(H_2)/P(H_2O)$ = 90/10) at 750 °C, i = +0.5 $A.cm^{-2}$ and with an inlet gas flux of 6 $NmL.min^{-1}.cm^{-2}$ for: (a) H_2O molecules on Ni surface, (b) H_2O molecules on YSZ surface, (c) OH^- ions on YSZ surface, (d) free sites on YSZ surface, (e) hydrogen ad atom on Ni surface, and (f) free sites on Ni surface.

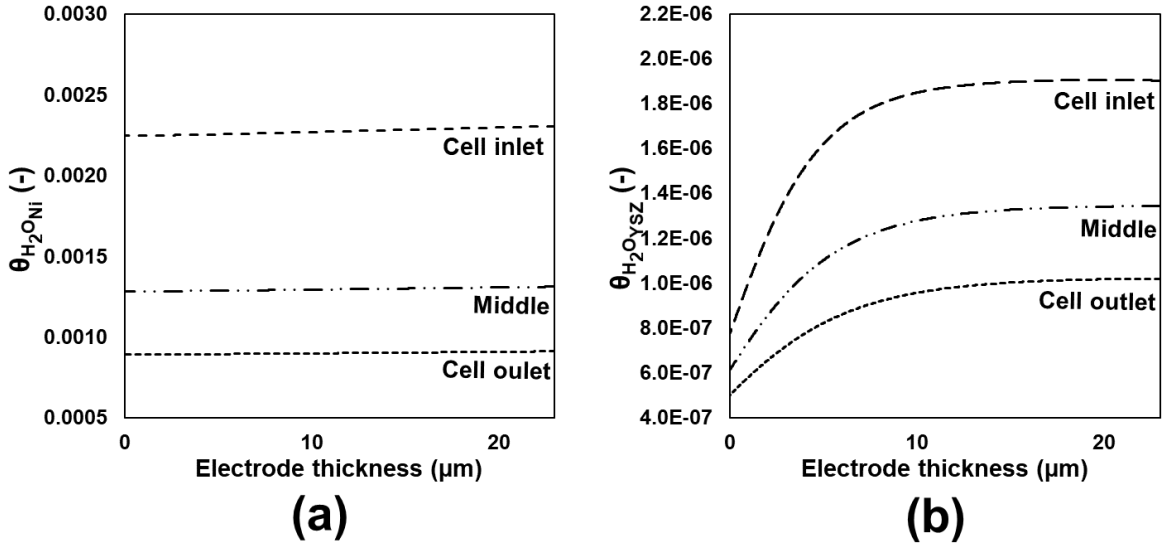

Figure 12 – Evolution of the surface coverage on YSZ and Ni surfaces in SOEC mode ($P(H_2)/P(H_2O)$ = 10/90) at 750 °C, i = -0.5 $A.cm^{-2}$ and with an inlet gas flux of 6 $NmL.min^{-1}.cm^{-2}$ for: (a) H_2O molecules on Ni surface, (b) H_2O molecules on YSZ surface.

5.3 Reaction mechanism in the air electrode

The local electronic current densities in LSCF and the sum of the ionic current densities in LSCF and CGO have been taken from the simulated dataset for an operation at 750°C and a cell current of ± 0.5 A.cm^{-2} in SOFC/SOEC mode. The profiles in the electrode thickness are plotted in Fig. 13a (SOFC) and 13b (SOEC) for the cell inlet, middle and outlet. With the microstructure of the studied LSCF-CGO composite, the reaction zone in the functional layer spreads over a limited distance of a few micrometers and does not exceed 10 µm in electrolysis mode (Fig. 13a). Moreover, as for the fuel electrode, the repartition of the local current densities is not significantly impacted by the position along the cell radius. It can be also noticed that the thickness of the reaction zone in fuel cell mode is roughly similar to the one in SOEC mode. Indeed, in this case, the reaction mechanism remains identical for both polarizations as detailed hereafter.

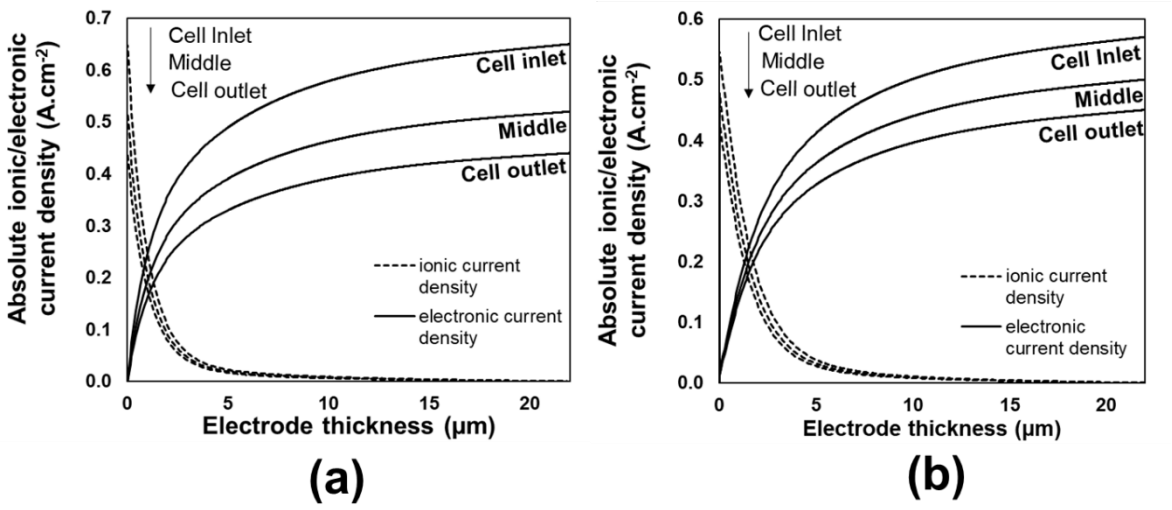

Figure 13 –Distribution of the ionic and electronic currents along the cell thickness for different radial positions with an inlet gas flux of 41 NmL.min^{-1}.cm^{-2}, T = 750 °C and P(O_2)/P(N_2) = 50/50 in (a) SOFC mode (i = +0.5 A.cm^{-2}) and (b) SOEC mode (-0.5 A.cm^{-2}).

The multiscale model has been also applied to analyze the activated reaction mechanism depending on the position along the cell radius. For this purpose, the ratio between the surface to the bulk path has been defined as follows [28]:

$$\zeta(r) = \frac{\int_{z=0}^{z=FL} v_{R10}(z,r)dz}{\int_{z=0}^{z=FL} v_{R9}(z,r)dz} \quad (7)$$

where v_{R9} and v_{R10} denote the kinetic rates for the reactions R9 and R10, respectively (Table 1). When $\zeta > 1$, the mechanism is mainly controlled by the surface path related to the charge transfer at TPBls, whereas $\zeta < 1$ means that the mechanism is governed by the bulk path related to the oxygen incorporation/excorporation at the LSCF surface.

The ratio ζ is plotted as function of the cell radius in Fig. 14a and 14b for a cell operated in SOFC and SOEC modes, respectively (at 750°C and i=+/-0.5 A.cm^{-2}). Whatever the position in the cell, it can be noted that the mechanism is completely dominated by the surface path ($\zeta > 1$) for both operating modes. This result is explained by the high density of active TPBls in the LSCF-CGO composite that favors the surface path [26], [28].

Under SOEC mode, it can be observed that the ratio decreases in the direction of the cell outlet (Fig. 14b). This evolution is driven by the concentration of incorporated oxygen atoms in the LSCF that has been computed from the inlet to the cell outlet. As shown in Fig. 14d, this concentration decreases along the cell length due to the decrease of the local current density (cf. Fig. 7). Therefore, the lower concentration of oxygen atom in LSCF, which is directly related to a higher concentration of vacancies, tends to promote the bulk path as already detailed in [28]. Under SOFC mode, the opposite behavior is observed. The oxygen reduction at the TPBls (i.e. surface path) is promoted at the cell outlet compared to the cell inlet (Fig. 14a). This behavior is linked to the increase in the concentration of incorporated oxygen in the direction of the cell outlet as shown in Fig. 14c [14].

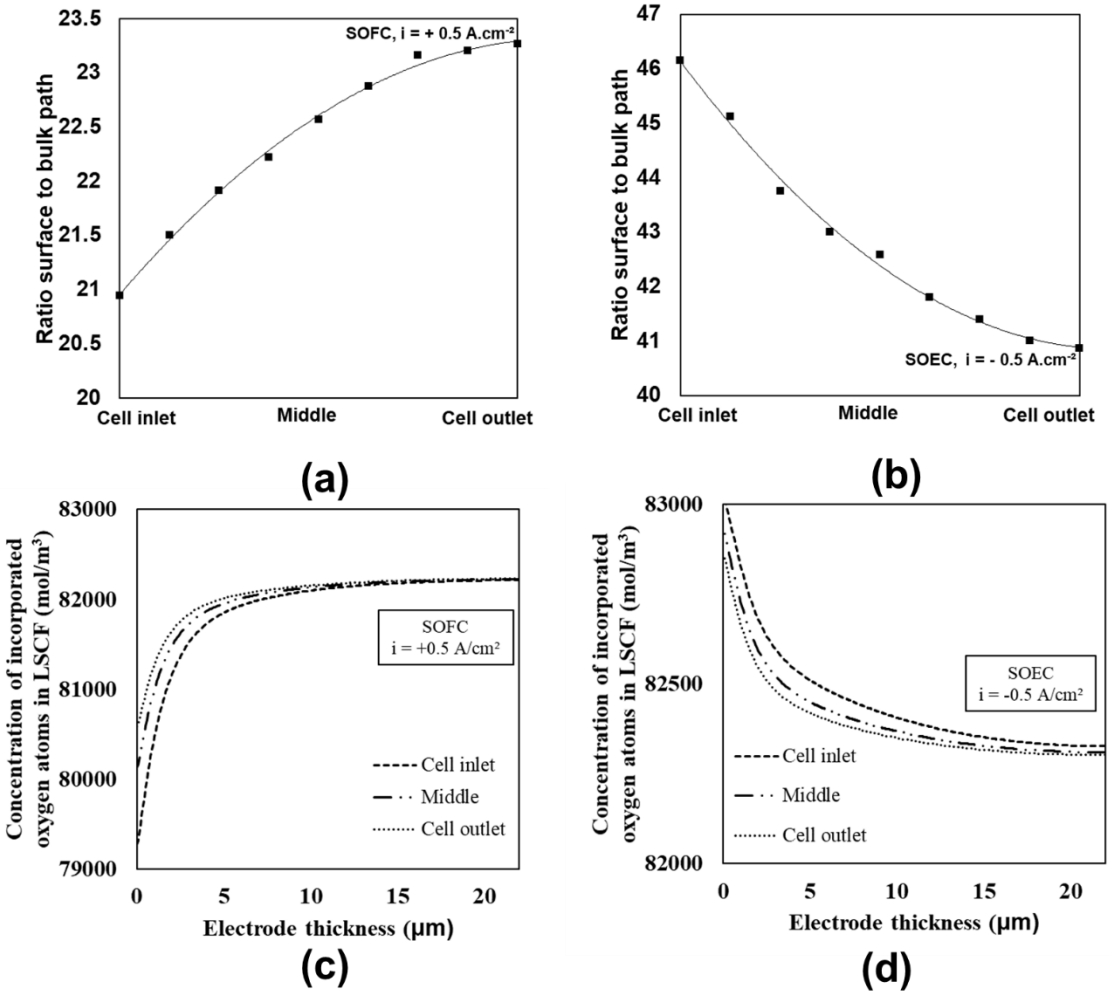

Figure 14 – Ratio between the surface and bulk pathways along the functional layer thickness for different regions of the cell radius at 750 °C and inlet flux of 41 NmL.min^{-1}cm^{-2} in (a) SOFC mode (i = +0.5 A.cm^{-2}) and (b) SOEC mode (i = -0.5 A.cm^{-2}). Concentration of oxygen atoms incorporated in LSCF along the functional layer thickness for different regions of the cell radius at 750 °C and inlet flux of 41 NmL.min^{-1}cm^{-2} in (c) SOFC mode (i = +0.5 A.cm^{-2}) and (d) SOEC mode (i = -0.5 A.cm^{-2}).

6. Conclusion

A coupled experimental and numerical approach has been adopted to elucidate the complex relationships between the global SOC response and the reaction mechanisms taking place in the electrodes. To perform this study, an in-house multiscale model has been developed and validated. This physical-based model consists of a combination of three different length-scales. The first module is devoted to the generation of synthetic microstructures for the morphological description of both electrodes. The second module describes all the

microscopic processes arising in the electrodes functional layers. They take into account the reaction mechanisms divided in elementary steps together with the mass and charge transfer in the electrode phases. These kinetic models are linked to the third module that allows the simulation of the global cell response. The multiscale model offers the possibility to study the impact of the cell design on the local distribution of reaction kinetic rates, current densities, gas composition, etc.

To validate the multiscale model, a special setup has been developed to measure the local polarization curves along the cell length. For this purpose, a specific design of the interconnect has been proposed in order to probe the local current density in the cell without any segmentation of the electrodes. This setup has been used to characterize a typical cell made of the classical SOCs materials (i.e. Ni-YSZ//YSZ//LSCF-CGO). Global and local polarization curves have been recorded in both SOFC and SOEC modes between 700 °C and 800 °C and for a large range of inlet flux for the fuel electrode (3-12 $NmL.min^{-1}.cm^{-2}$). As expected, it has been found that the cell performances are improved with increasing the H_2/H_2O inlet flux and the temperature. The local measurements have confirmed that the local current density decreases along the cell length from the inlet to the outlet.

The cell response has been computed with the model in the same conditions than the experiments. For this purpose, the model has been applied to the studied cell by considering an accurate description of the electrode microstructures. It has been found that the model is able to simulate accurately the global and local polarization curves obtained in SOFC and SOEC modes. A good agreement has been found between the simulated local current densities and the ones measured along the cell for various cell voltages. These results constitute a cross validation of the model and the specific setup proposed to measure the local current densities.

The model has been applied to study the fuel and air electrode operation as a function of the cell length. For the fuel electrode, it has been highlighted that the extension of the reactions in the functional layer is almost independent on the position along the cell length. However, the reaction mechanism evolves continuously from the cell inlet to the outlet. In SOEC mode, this evolution leads to a change in the mechanism. Indeed, the steam molecules adsorb preferentially on the Ni surface at the inlet; whereas the adsorption on YSZ becomes dominant at the outlet. In SOFC mode, the steam interaction with YSZ surface is favored whatever the position, although the contribution of the Ni surface on the reaction pathways is enhanced along the cell length. All these evolutions have been discussed and explained with the distribution of adsorbates on both surfaces. Regarding the air electrode, it has been also

found that the thickness of the reaction zone in the functional layer is almost the same along the cell length. Moreover, the reaction mechanism remains mainly controlled by the so-called surface path related to the charge transfer at the TPBls. Nevertheless, in SOEC mode, the relative weight of the bulk path associated to the charge transfer at the LSCF surface is increased along the cell length. The opposite trend has been found in SOFC mode. These evolutions have been explained by the change of oxygen content in the LSCF material.

7. Acknowledgments

The research leading to these results has received funding from Fuel cells and Hydrogen Joint Undertaking under Grant Agreement n° 875047 (RUBY Project), grand agreement n° 101007175 (REACTT project) and grant agreement n° 874577 (NewSOC project). The work has also been supported by Genvia and the project CELCER-EHT.

8. Nomenclature

Roman symbols

A	Exchange density pre-exponential factor in the hydrogen electrode, (A.cm^{-2})
B	Exchange density pre-exponential factor in the air electrode, (A.cm^{-2})
$C_{O_\delta^\times}^{max.}$	Maximum concentration of oxygen incorporated in LSCF, (mol.m^{-3})
E_a^i	Activation energy of the exchange current density for the electrode *i*, (J.mol^{-1})
$E_{i=0}$	Open circuit voltage, (V)
e^-	Electron, (-)
F	Faraday's constant, (C.mol^{-1})
i	Cell current density, (A.cm^{-2})
i_{io}	Local ionic current density, (A.cm^{-2})
i_{el}	Local electronic current density, (A.cm^{-2})
i_0^i	Exchange current density in the electrode *i*, (A.cm^{-2})
k	Kinetic constant of the reaction, (units shown in Table 1)
m	Exchange density exponent for the hydrogen partial pressure, (-)
n	Exchange density exponent for the steam partial pressure, (-)
p	Exchange density exponent for the oxygen partial pressure, (-)
p_i	Partial pressure of the specie *i*, (atm)
R	Universal gas constant, (J.mol^{-1}.K^{-1})
R_c	Contact resistance, (Ω.cm^2)
$\overline{r_i}$	Radius of the phase i, (µm)
s_i	Free site on the surface for the phase *i* (-)
Sp_{i-j}	Specific surface area between phase *i* and *j*, (µm^{-1})
T	Absolut temperature, (K)
U_{cell}	Cell voltage, (V)

Chemical species

$H_2(g)$	Gaseous hydrogen, (-)
$H_2O(g)$	Gaseous water, (-)
H_{Ni}	H attached on Ni surface, (-)
H_2O_{Ni}	H_2O attached on Ni surface, (-)
H_2O_{YSZ}	H_2O attached on YSZ surface, (-)
$h^{\bullet}$	Hole defect in the LSCF, (-)
$O_2(g)$	Gaseous oxygen
O_{YSZ}^{2-}	O^{2-} attached on YSZ surface, (-)
$O_O^x(YSZ)$	Oxygen in the YSZ lattice, (-)
OH_{YSZ}^-	OH^- attached on YSZ surface, (-)
$O_O^x(CGO)$	Oxygen in CGO lattice
$O_O^x(LSCF)$	Oxygen in LSCF lattice
O_{LSCF}^-	Oxygen ad-ion on the LSCF surface
O_{LSCF}	Oxygen ad-atom on the LSCF surface
$O_{2_{LSCF}}$	Oxygen ad-molecule on the LSCF surface
$V_O^{\bullet\bullet}(YSZ)$	Oxygen vacancies in the YSZ lattice, (-)
$V_O^{\bullet\bullet}(LSCF)$	Oxygen vacancy in the LSCF lattice, (-)
$V_O^{\bullet\bullet}(CGO)$	Oxygen vacancy in the CGO lattice, (-)

Greek symbols

ε_i	Volume fraction of the phase *i*, (-)
ζ	Ratio between surface and bulk path, (-)
ξ	Ratio between steam adsorption/desorption on Ni and YSZ, (-)
ξ_{TPB}	Triple phase boundary length density, (μm^{-2})
η_{conc}^i	Concentration overpotential in the electrode *i*, (V)
η_{act}^i	Activation overpotential in the electrode *i*, (V)
η_{ohm}	Ohmic overpotential, (V)
η_{diff}	Gas diffusion overpotential, (V)
η_{conv}	Gas conversion overpotential, (V)
θ_{i_j}	Local coverage of the specie *i* on the surface of the phase *j*, (-)
τ_i	Tortuosity factor of the phase *i*, (-)

9. List of Abbreviations

3YSZ	Yttria Stabilized Zirconia with 3.mol% of Yttria
8YSZ	Yttria Stabilized Zirconia with 8.mol% of Yttria
CGO	Gadolinium-doped Ceria
DGM	Dusty Gas Model
EIS	Electrochemical Impedance Spectroscopy
HTSE	High-Temperature Steam Electrolysis
LSCF	Lanthanum Strontium Cobalt Ferrite
MIEC	Mixed Ionic and Electronic Conductor
OCV	Open Circuit Voltage
RVE	Representative Volume Element
SOCs	Solid Oxide Cells
SOEC	Solid Oxide Electrolysis Cell
SOFC	Solid Oxide Fuel Cell
SRU	Single Repeating Unit
YSZ	Yttria Stabilized Zirconia

10. References

[1] A. Godula-Jopek, *Hydrogen Production by Electrolysis*. 2015.

[2] J. Aicart, Z. Wuillemin, B. Gervasoni, D. Reynaud, F. Waeber, C. Beetschen, Y. Antonetti, A. Nesci, and J. Mougin, "Performance evaluation of a 4-stack solid oxide module in electrolysis mode," *Int. J. Hydrogen Energy*, vol. 47, no. 6, pp. 3568–3579, Jan. 2022, doi: 10.1016/j.ijhydene.2021.11.056.

[3] F. Monaco, D. Ferreira-Sanchez, M. Hubert, B. Morel, D. Montinaro, D. Grolimund, and J. Laurencin, "Oxygen electrode degradation in solid oxide cells operating in electrolysis and fuel cell modes: LSCF destabilization and interdiffusion at the electrode/electrolyte interface," *Int. J. Hydrogen Energy*, vol. 46, no. 62, pp. 31533–31549, Sep. 2021, doi: 10.1016/j.ijhydene.2021.07.054.

[4] E. Da Rosa Silva, M. Hubert, B. Morel, H. Moussaoui, J. Debayle, and J. Laurencin, "A Dynamic Multi-Scale Model for Solid Oxide Cells Validated on Local Current Measurements: Impact of Global Cell Operation on the Electrodes Reaction Mechanisms," *ECS Meet. Abstr.*, vol. MA2021-03, no. 1, pp. 164–164, 2021, doi: 10.1149/ma2021-031164mtgabs.

[5] S. J. McPhail, S. Frangini, J. Laurencin, E. Effori, A. Abaza, A. K. Padinjarethil, A. Hagen, A. Léon, A. Brisse, D. Vladikova, B. Burdin, F. R. Bianchi, B. Bosio, P. Piccardo, R. Spotorno, H. Uchida, P. Polverino, E. A. Adinolfi, F. Postiglione, J. Lee, H. Moussaoui, J . Van Herle, "Addressing planar solid oxide cell degradation mechanisms: A critical review of selected components," *Electrochem. Sci. Adv.*, no. February, pp. 1–37, Nov. 2021, doi: 10.1002/elsa.202100024.

[6] Q. Cai, C. S. Adjiman, and N. P. Brandon, "Optimal control strategies for hydrogen production when coupling solid oxide electrolysers with intermittent renewable energies," *J. Power Sources*, vol. 268, pp. 212–224, 2014, doi: 10.1016/j.jpowsour.2014.06.028.

[7] S. B. Beale, M. Andersson, C. Boigues-Muñoz, H. L. Frandsen, Z. Lin, S. J. McPhail, M. Ni, B. Sundén, A. Weber, and A. Z. Weber, "Continuum scale modelling and complementary experimentation of solid oxide cells," *Prog. Energy Combust. Sci.*, vol. 85, p. 100902, 2021, doi: 10.1016/j.pecs.2020.100902.

[8] A. Nechache and S. Hody, "Alternative and innovative solid oxide electrolysis cell materials: A short review," *Renew. Sustain. Energy Rev.*, vol. 149, 2021, doi: 10.1016/j.rser.2021.111322.

[9] A. Nechache, M. Cassir, and A. Ringuedé, "Solid oxide electrolysis cell analysis by means of electrochemical impedance spectroscopy : A review," *J. Power Sources*, vol. 258, pp. 164–181, 2014, doi: 10.1016/j.jpowsour.2014.01.110.

[10] C. H. J. UNDERTAKING, "Strategic Research and Innovation Agenda for RHC, 2013," *Decis. no. CleanHydrogen-GB-2022-02*, 2020, doi: 10.13140/2.1.4252.7520.

[11] S. D. Vora, W. L. Lundberg, and J. F. Pierre, "Overview of U.S. Department of Energy Office of Fossil Energy's Solid Oxide Fuel Cell Program," *ECS Trans.*, vol. 78, pp. 3-19, 2017, doi: 10.1149/07801.0003ecst.

[12] Q. Fang, L. Blum, and D. Stolten, "Electrochemical Performance and Degradation Analysis of an SOFC Short Stack Following Operation of More than 100,000 Hours," *J. Electrochem. Soc.*, vol. 166, no. 16, pp. F1320–F1325, 2019, doi: 10.1149/2.0751916jes.

[13] Y. Wang, W. Li, L. Ma, W. Li, and X. Liu, "Degradation of solid oxide electrolysis cells: Phenomena, mechanisms, and emerging mitigation strategies—A review," *J.*

Mater. Sci. Technol., vol. 55, pp. 35–55, 2020, doi: 10.1016/j.jmst.2019.07.026.

[14] J. Laurencin, M. Hubert, D. F. Sanchez, S. Pylypko, M. Morales, A. Morata, B. Morel, D. Montinaro, F. Lefebvre-Joud, and E. Siebert, "Degradation mechanism of La0.6Sr0.4Co0.2Fe0.8O3-δ/Gd0.1Ce0.9O2-δ composite electrode operated under solid oxide electrolysis and fuel cell conditions," *Electrochim. Acta*, vol. 241, pp. 459–476, 2017, doi: 10.1016/j.electacta.2017.05.011.

[15] P. Metzger, K. A. Friedrich, H. Müller-Steinhagen, and G. Schiller, "SOFC characteristics along the flow path," *Solid State Ionics*, vol. 177, no. 19-25 SPEC. ISS., pp. 2045–2051, 2006, doi: 10.1016/j.ssi.2006.06.019.

[16] F. Ravussin, J. Van herle, N. Autissier, M. Molinelli, D. Larrain, and D. Favrat, "Local current measurement in a solid oxide fuel cell repeat element," *J. Eur. Ceram. Soc.*, vol. 27, no. 2–3, pp. 1035–1040, 2007, doi: 10.1016/j.jeurceramsoc.2006.05.089.

[17] W. G. Bessler, S. Gewies, C. Willich, G. Schiller, and K. A. Friedrich, "Spatial distribution of electrochemical performance in a segmented SOFC: A combined modeling and experimental study," *Fuel Cells*, vol. 10, no. 3, pp. 411–418, 2010, doi: 10.1002/fuce.200900083.

[18] P. Tanasini, J. A. Schuler, Z. Wuillemin, M. L. B. Ameur, C. Comninellis, and J. Van Herle, "Segmented cell testing for cathode parameter investigation," *J. Power Sources*, vol. 196, no. 17, pp. 7097–7103, 2011, doi: 10.1016/j.jpowsour.2010.08.034.

[19] Z. Wuillemin, Y. Antonetti, C. Beetschen, O. Millioud, S. Ceschini, H. Madi, and J. Van herle, "Local Activation and Degradation of Electrochemical Processes in a SOFC," *ECS Trans.*, vol. 57, no. 1, pp. 561–570, 2013, doi: 10.1149/05701.0561ecst.

[20] Ö. Aydın, H. Nakajima, and T. Kitahara, "Reliability of the numerical SOFC models for estimating the spatial current and temperature variations," *Int. J. Hydrogen Energy*, vol. 41, no. 34, pp. 15311–15324, 2016, doi: 10.1016/j.ijhydene.2016.06.194.

[21] B. Conti, B. Bosio, S. J. McPhail, F. Santoni, D. Pumiglia, and E. Arato, "A 2-D model for intermediate temperature solid oxide fuel cells preliminarily validated on local values," *Catalysts*, vol. 9, no. 1, 2019, doi: 10.3390/catal9010036.

[22] J. A. Schuler, H. Yokokawa, C. F. Calderone, Q. Jeangros, Z. Wuillemin, A. Hessler-Wyser, and J. Van Herle, "Combined Cr and S poisoning in solid oxide fuel cell

cathodes," *J. Power Sources*, vol. 201, pp. 112–120, 2012, doi: 10.1016/j.jpowsour.2011.10.123.

[23] A. Donazzi, S. De Pascali, F. Garavaglia, and M. Bracconi, "A quasi 2D model for the interpretation of impedance and polarization of a planar solid oxide fuel cell with interconnects," *Electrochim. Acta*, vol. 365, p. 137346, 2021, doi: 10.1016/j.electacta.2020.137346.

[24] H. Moussaoui, J. Laurencin, Y. Gavet, G. Delette, M. Hubert, P. Cloetens, T. Le Bihan, and J. Debayle, "Stochastic geometrical modeling of solid oxide cells electrodes validated on 3D reconstructions," *Comput. Mater. Sci.*, vol. 143, pp. 262–276, 2018, doi: 10.1016/j.commatsci.2017.11.015.

[25] H. Moussaoui, J. Laurencin, M. Hubert, R. Sharma, P. Cloetens, G. Delette, Y. Gavet, and J. Debayle, "Stochastic Geometrical and Microstructural Modeling for Solid Oxide Cell Electrodes," *ECS Trans.*, vol. 91, no. 1, pp. 2031–2043, 2019, doi: 10.1149/09101.2031ecst.

[26] E. Effori, H. Moussaoui, F. Monaco, R. K. Sharma, J. Debayle, Y. Gavet, G. Delette, G. Si Larbi, E. Siebert, J. Vulliet, L. Dessemond, and J. Laurencin, "Reaction Mechanism and Impact of Microstructure on Performances for the LSCF-CGO Composite Electrode in Solid Oxide Cells," *Fuel Cells*, vol. 19, no. 4, pp. 429–444, 2019, doi: 10.1002/fuce.201800185.

[27] M. Hubert, J. Laurencin, P. Cloetens, J. C. da Silva, F. Lefebvre-Joud, P. Bleuet, A. Nakajo, and E. Siebert, "Role of microstructure on electrode operating mechanisms for mixed ionic electronic conductors: From synchrotron-based 3D reconstruction to electrochemical modeling," *Solid State Ionics*, vol. 294, pp. 90–107, 2016, doi: 10.1016/j.ssi.2016.07.001.

[28] E. Effori, J. Laurencin, E. D. R. Silva, M. Hubert, T. David, M. Petitjean, G. Geneste, L. Dessemond, and E. Siebert, "An Elementary Kinetic Model for the LSCF and LSCF-CGO Electrodes of Solid Oxide Cells: Impact of Operating Conditions and Degradation on the Electrode Response," *J. Electrochem. Soc.*, vol. 168, no. 4, p. 044520, 2021, doi: 10.1149/1945-7111/abf40a.

[29] S. Gewies and W. G. Bessler, "Physically Based Impedance Modeling of Ni/YSZ Cermet Anodes," *J. Electrochem. Soc.*, vol. 155, no. 9, p. B937, 2008, doi:

10.1149/1.2943411.

[30] A. Donazzi, G. Cordaro, A. Baricci, Z. Bin Ding, and M. Maestri, "A detailed kinetic model for the reduction of oxygen on LSCF-GDC composite cathodes," *Electrochim. Acta*, vol. 335, p. 135620, 2020, doi: 10.1016/j.electacta.2020.135620.

[31] J. Laurencin, D. Kane, G. Delette, J. Deseure, and F. Lefebvre-Joud, "Modelling of solid oxide steam electrolyser: Impact of the operating conditions on hydrogen production," *J. Power Sources*, vol. 196, no. 4, pp. 2080–2093, 2011, doi: 10.1016/j.jpowsour.2010.09.054.

[32] L. Bernadet, J. Laurencin, G. Roux, D. Montinaro, F. Mauvy, and M. Reytier, "Effects of Pressure on High Temperature Steam and Carbon Dioxide Co-electrolysis," *Electrochim. Acta*, vol. 253, pp. 114–127, 2017, doi: 10.1016/j.electacta.2017.09.037.

[33] O. Babaie Rizvandi, X. Y. Miao, and H. L. Frandsen, "Multiscale modeling of degradation of full solid oxide fuel cell stacks," *Int. J. Hydrogen Energy*, vol. 46, no. 54, pp. 27709–27730, 2021, doi: 10.1016/j.ijhydene.2021.05.204.

[34] R. T. Nishida, S. B. Beale, J. G. Pharoah, L. G. J. de Haart, and L. Blum, "Three-dimensional computational fluid dynamics modelling and experimental validation of the Jülich Mark-F solid oxide fuel cell stack," *J. Power Sources*, vol. 373, no. July 2017, pp. 203–210, 2018, doi: 10.1016/j.jpowsour.2017.10.030.

[35] M. Navasa, X. Y. Miao, and H. L. Frandsen, "A fully-homogenized multiphysics model for a reversible solid oxide cell stack," *Int. J. Hydrogen Energy*, vol. 44, no. 41, pp. 23330–23347, 2019, doi: 10.1016/j.ijhydene.2019.06.077.

[36] M. Andersson, J. Yuan, and B. Sundén, "Review on modeling development for multiscale chemical reactions coupled transport phenomena in solid oxide fuel cells," *Appl. Energy*, vol. 87, no. 5, pp. 1461–1476, 2010, doi: 10.1016/j.apenergy.2009.11.013.

[37] L. Mastropasqua, A. Donazzi, and S. Campanari, "Development of a Multiscale SOFC Model and Application to Axially-Graded Electrode Design," *Fuel Cells*, vol. 19, no. 2, pp. 125–140, 2019, doi: 10.1002/fuce.201800170.

[38] H. Zhu, R. J. Kee, V. M. Janardhanan, O. Deutschmann, and D. G. Goodwin, "Modeling Elementary Heterogeneous Chemistry and Electrochemistry in Solid-Oxide

Fuel Cells," *J. Electrochem. Soc.*, vol. 152, no. 12, p. A2427, 2005, doi: 10.1149/1.2116607.

[39] A. Bertei, J. Mertens, and C. Nicolella, "Electrochemical simulation of planar solid oxide fuel cells with detailed microstructural modeling," *Electrochim. Acta*, vol. 146, pp. 151–163, 2014, doi: 10.1016/j.electacta.2014.08.120.

[40] M. Mozdzierz, K. Berent, S. Kimijima, J. S. Szmyd, and G. Brus, "A multiscale approach to the numerical simulation of the solid oxide fuel cell," *Catalysts*, vol. 9, no. 3, pp. 1–27, 2019, doi: 10.3390/catal9030253.

[41] G. Schiller, W. G. Bessler, K. A. Friedrich, S. Gewies, and C. Willich, "Spatially Resolved Electrochemical Performance in a Segmented Planar SOFC," *ECS Trans.*, vol. 17, no. 1, pp. 79–87, 2009, doi: 10.1149/1.3142737.

[42] M. Lang, C. Auer, G. Braniek, F. Wenz, and F. Hauler, "Understanding the Electrochemical Performance of SOFC Stacks," *ECS Meet. Abstr.*, vol. MA2015-03, no. 1, pp. 352–352, 2015, doi: 10.1149/ma2015-03/1/352.

[43] M. Lang, C. Bohn, M. Henke, G. Schiller, C. Willich, and F. Hauler, "Understanding the Current-Voltage Behavior of High Temperature Solid Oxide Fuel Cell Stacks," *J. Electrochem. Soc.*, vol. 164, no. 13, pp. F1460–F1470, 2017, doi: 10.1149/2.1541713jes.

[44] W. G. Bessler, S. Gewies, and M. Vogler, "A new framework for physically based modeling of solid oxide fuel cells," *Electrochim. Acta*, vol. 53, no. 4, pp. 1782–1800, 2007, doi: 10.1016/j.electacta.2007.08.030.

[45] G. Rinaldi, A. Nakajo, J. Van herle, P. Burdet, E. Oveisi, and M. Cantoni, "Strontium Migration at the GDC-YSZ Interface of Solid Oxide Cells in SOFC and SOEC Modes," *ECS Meet. Abstr.*, vol. MA2017-03, no. 1, pp. 299–299, 2017, doi: 10.1149/ma2017-03/1/299.

[46] J. P. Serra, *Image Analysis and Mathematical Morphology: Theoretical advances*. Academic Press, 1982. [Online]. Available: https://books.google.fr/books?id=SfF4zgEACAAJ

[47] J. Laurencin, M. Hubert, K. Couturier, T. Le Bihan, P. Cloetens, F. Lefebvre-Joud, and E. Siebert, "Reactive Mechanisms of LSCF Single-Phase and LSCF-CGO Composite

Electrodes Operated in Anodic and Cathodic Polarisations," *Electrochim. Acta*, vol. 174, pp. 1299–1316, 2015, doi: 10.1016/j.electacta.2015.06.080.

[48] F. Monaco, E. Effori, M. Hubert, E. Siebert, G. Geneste, B. Morel, E. Djurado, D. Montinaro, and J. Laurencin, "Electrode kinetics of porous Ni-3YSZ cermet operated in fuel cell and electrolysis modes for solid oxide cell application," *Electrochim. Acta*, vol. 389, pp. 1–53, 2021, doi: 10.1016/j.electacta.2021.138765.

[49] D. G. Goodwin, H. Zhu, A. M. Colclasure, and R. J. Kee, "Modeling Electrochemical Oxidation of Hydrogen on Ni–YSZ Pattern Anodes," *J. Electrochem. Soc.*, vol. 156, no. 9, p. B1004, 2009, doi: 10.1149/1.3148331.

[50] M. Hubert, A. Pacureanu, C. Guilloud, Y. Yang, J. C. Da Silva, J. Laurencin, F. Lefebvre-Joud, and P. Cloetens, "Efficient correction of wavefront inhomogeneities in X-ray holographic nanotomography by random sample displacement," *Appl. Phys. Lett.*, vol. 112, no. 20, 2018, doi: 10.1063/1.5026462.

[51] H. Moussaoui, J. Debayle, Y. Gavet, P. Cloetens, and J. Laurencin, "Particle-based model for functional and diffusion layers of solid oxide cells electrodes," *Powder Technol.*, vol. 367, pp. 67–81, 2020, doi: 10.1016/j.powtec.2020.03.040.

[52] A. Yahya, D. Ferrero, H. Dhahri, P. Leone, K. Slimi, and M. Santarelli, "Electrochemical performance of solid oxide fuel cell: Experimental study and calibrated model," *Energy*, vol. 142, pp. 932–943, 2018, doi: 10.1016/j.energy.2017.10.088.

[53] D. Kanno, N. Shikazono, N. Takagi, K. Matsuzaki, and N. Kasagi, "Evaluation of SOFC anode polarization simulation using three-dimensional microstructures reconstructed by FIB tomography," *Electrochim. Acta*, vol. 56, no. 11, pp. 4015–4021, 2011, doi: 10.1016/j.electacta.2011.02.010.

[54] T. Fukumoto, N. Endo, K. Mori, Y. Tachikawa, J. Matsuda, S. Taniguchi, and K. Sasaki, "Exchange Current Density of Solid Oxide Electrolysis Cell Electrodes," *ECS Meet. Abstr.*, vol. MA2021-03, no. 1, pp. 282–282, 2021, doi: 10.1149/ma2021-031282mtgabs.

[55] P. Costamagna, A. Selimovic, M. D. Borghi, G. Agnew, "Electrochemical model of the integrated planar solid oxide fuel cell (IP-SOFC)," *J. Chem. Eng.*, vol. 102, no. 1, pp 61-69, 2004, doi: 10.1016/j.cej.2004.02.005

[56] J. Udagawa, P. Aguiar, N. P. Brandon, "Hydrogen production through steam electrolysis: Model-based steady state performance of a cathode-supported intermediate temperature solid oxide electrolysis cell," *J. Power Sources*, vol. 166, no. 1, pp. 127-136, 2007, https://doi.org/10.1016/j.jpowsour.2006.12.081.

[57] E. Effori, J. Laurencin, V. Tezyk, C. Montella, L. Dessemond, and E. Siebert, "A physically-based modelling to predict the cyclic voltammetry response of LSCF-type electrodes: Impact of the Ohmic Losses and Microstructure," *Solid State Ionics*, vol. 371, no. August, p. 115765, 2021, doi: 10.1016/j.ssi.2021.115765.

[58] M. Reytier, S. Di Iorio, A. Chatroux, M. Petitjean, J. Cren, M. De Saint Jean, J. Aicart, and J. Mougin, "Stack performances in high temperature steam electrolysis and co-electrolysis," *Int. J. Hydrogen Energy*, vol. 40, no. 35, pp. 11370–11377, 2015, doi: 10.1016/j.ijhydene.2015.04.085.

[59] M. Ni, M. K. H. Leung, and D. Y. C. Leung, "Parametric study of solid oxide fuel cell performance," *Energy Convers. Manag.*, vol. 48, no. 5, pp. 1525–1535, 2007, doi: 10.1016/j.enconman.2006.11.016.

[60] J. Laurencin, G. Delette, B. Morel, F. Lefebvre-Joud, and M. Dupeux, "Solid Oxide Fuel Cells damage mechanisms due to Ni-YSZ re-oxidation: Case of the Anode Supported Cell," *J. Power Sources*, vol. 192, no. 2, pp. 344–352, 2009, doi: 10.1016/j.jpowsour.2009.02.089.

[61] F. Usseglio-Viretta, J. Laurencin, G. Delette, J. Villanova, P. Cloetens, and D. Leguillon, "Quantitative microstructure characterization of a Ni-YSZ bi-layer coupled with simulated electrode polarisation," *J. Power Sources*, vol. 256, pp. 394–403, 2014, doi: 10.1016/j.jpowsour.2014.01.094.